arXiv:1310.7583v1 [astro-ph.CO] 28 Oct 2013

# HERMES: CANDIDATE HIGH-REDSHIFT GALAXIES DISCOVERED WITH *HERSCHEL*/SPIRE[†]

C. Darren Dowell[1,2], A. Conley[3], J. Glenn[4,3], V. Arumugam[5], V. Asboth[6], H. Aussel[7], F. Bertoldi[8], M. Béthermin[7], J. Bock[1,2], A. Boselli[9], C. Bridge[1], V. Buat[9], D. Burgarella[9], A. Cabrera-Lavers[10,11,12], C.M. Casey[13], S.C. Chapman[14,15], D.L. Clements[16], L. Conversi[17], A. Cooray[18,1], H. Dannerbauer[19], F. De Bernardis[18], T.P. Ellsworth-Bowers[4], D. Farrah[20], A. Franceschini[21], M. Griffin[22], M.A. Gurwell[23], M. Halpern[6], E. Hatziminaoglou[24], S. Heinis[9], E. Ibar[25,26], R.J. Ivison[25,5], N. Laporte[10,11], L. Marchetti[27,21], P. Martínez-Navajas[10,11], G. Marsden[6], G.E. Morrison[13,28], H.T. Nguyen[2,1], B. O'Halloran[16], S.J. Oliver[29], A. Omont[30], M.J. Page[31], A. Papageorgiou[22], C.P. Pearson[32,27], G. Petitpas[23], I. Pérez-Fournon[10,11], M. Pohlen[22], D. Riechers[33,1], D. Rigopoulou[32,34], I.G. Roseboom[29,5], M. Rowan-Robinson[16], J. Sayers[1], B. Schulz[1,35], Douglas Scott[6], N. Seymour[36], D.L. Shupe[1,35], A.J. Smith[29], A. Streblyanska[10,11], M. Symeonidis[31], M. Vaccari[21,37], I. Valtchanov[17], J.D. Vieira[1], M. Viero[1], L. Wang[29], J. Wardlow[18], C.K. Xu[1,35], M. Zemcov[1]

## ABSTRACT

We present a method for selecting $z > 4$ dusty, star forming galaxies (DSFGs) using *Herschel*/SPIRE $250/350/500\,\mu m$ flux densities to search for red sources. We apply this method to 21 deg$^2$ of data from the HerMES survey to produce a catalog of 38 high-$z$ candidates. Follow-up of the first 5 of these sources confirms that this method is efficient at selecting high-$z$ DSFGs, with 4/5 at $z = 4.3$ to 6.3 (and the remaining source at $z = 3.4$), and that they are some of the most luminous dusty sources known. Comparison with previous DSFG samples, mostly selected at longer wavelengths (e.g., $850\,\mu m$) and in single-band surveys, shows that our method is much more efficient at selecting high-$z$ DSFGs, in the sense that a much larger fraction are at $z > 3$. Correcting for the selection completeness and purity, we find that the number of bright ($S_{500\mu m} \geq 30\,\mathrm{mJy}$), red *Herschel* sources is $3.3 \pm 0.8$ deg$^{-2}$. This is much higher than the number predicted by current models, suggesting that the DSFG population extends to higher redshifts than previously believed. If the shape of the luminosity function for high-$z$ DSFGs is similar to that at $z \sim 2$, rest-frame UV based studies may be missing a significant component of the star formation density at $z = 4$ to 6, even after correction for extinction.

*Subject headings:* galaxies:high-redshift; galaxies:starburst; submillimeter

[†] *Herschel* is an ESA space observatory with science instruments provided by European-led Principal Investigator consortia and with important participation from NASA.

[1] California Institute of Technology, 1200 E. California Blvd., Pasadena, CA 91125; cdd@phobos.caltech.edu

[2] Jet Propulsion Laboratory, 4800 Oak Grove Drive, Pasadena, CA 91109

[3] Center for Astrophysics and Space Astronomy 389-UCB, University of Colorado, Boulder, CO 80309

[4] Dept. of Astrophysical and Planetary Sciences, CASA 389-UCB, University of Colorado, Boulder, CO 80309

[5] Institute for Astronomy, University of Edinburgh, Royal Observatory, Blackford Hill, Edinburgh EH9 3HJ, UK

[6] Department of Physics & Astronomy, University of British Columbia, 6224 Agricultural Road, Vancouver, BC V6T 1Z1, Canada

[7] Laboratoire AIM-Paris-Saclay, CEA/DSM/Irfu - CNRS - Université Paris Diderot, CE-Saclay, pt courrier 131, F-91191 Gif-sur-Yvette, France

[8] Argelander Institute für Astronomie, Universität Bonn, Auf dem Hügel 71, 53121 Bonn, Germany

[9] Aix-Marseille Université, CNRS, LAM (Laboratoire d'Astrophysique de Marseille) UMR7326, 13388, France

[10] Instituto de Astrofísica de Canarias (IAC), E-38200 La Laguna, Tenerife, Spain

[11] Departamento de Astrofísica, Universidad de La Laguna (ULL), E-38205 La Laguna, Tenerife, Spain

[12] GTC Project, E-38205 La Laguna, Tenerife, Spain

[13] Institute for Astronomy, University of Hawaii, 2680 Woodlawn Drive, Honolulu, HI 96822

[14] Department of Physics and Atmospheric Science, Dalhousie University, Halifax, NS B3H 3J5, Canada

[15] Institute of Astronomy, University of Cambridge, Madingley Road, Cambridge CB3 0HA, UK

[16] Astrophysics Group, Imperial College London, Blackett

Laboratory, Prince Consort Road, London SW7 2AZ, UK

[17] Herschel Science Centre, European Space Astronomy Centre, Villanueva de la Cañada, 28691 Madrid, Spain

[18] Dept. of Physics & Astronomy, University of California, Irvine, CA 92697

[19] Universität Wien, Institut für Astrophysic, Türkenschanzstraße 17, 1180, Wien, Austria

[20] Department of Physics, Virginia Tech, Blacksburg, VA 24061

[21] Dipartimento di Fisica e Astronomia, Università di Padova, vicolo Osservatorio, 3, 35122 Padova, Italy

[22] School of Physics and Astronomy, Cardiff University, Queens Buildings, The Parade, Cardiff CF24 3AA, UK

[23] Harvard-Smithsonian Center for Astrophysics, 60 Garden Street, Cambridge, MA 02138

[24] ESO, Karl-Schwarzschild-Str. 2, 85748 Garching bei München, Germany

[25] UK Astronomy Technology Centre, Royal Observatory, Blackford Hill, Edinburgh EH9 3HJ, UK

[26] Universidad Católica de Chile, Departamento de Astronomía y Astrofísica, Vicuña Mackenna 4860, Casilla 306, Santiago 22, Chile

[27] Department of Physical Sciences, The Open University, Milton Keynes MK7 6AA, UK

[28] Canada-France-Hawaii Telescope, Kamuela, HI, 96743

[29] Astronomy Centre, Dept. of Physics & Astronomy, University of Sussex, Brighton BN1 9QH, UK

[30] Institut d'Astrophysique de Paris, UMR 7095, CNRS, UPMC Univ. Paris 06, 98bis boulevard Arago, F-75014 Paris, France

[31] Mullard Space Science Laboratory, University College London, Holmbury St. Mary, Dorking, Surrey RH5 6NT, UK

[32] RAL Space, Rutherford Appleton Laboratory, Chilton, Didcot, Oxfordshire OX11 0QX, UK

[33] Department of Astronomy, Space Science Building, Cornell

## 1. INTRODUCTION

The study of massive, dusty, star-forming galaxies (DSFGs) since their discovery more than a decade ago (Smail, Ivison, & Blain 1997; Hughes et al. 1998; Barger et al. 1998) has fundamentally changed our understanding of the cosmic history of star formation and galaxy evolution (e.g., Lagache, Puget, & Dole 2005). These sources are generally believed to be the progenitors of massive elliptical galaxies in the current epoch. They were first studied in the sub-mm and mm[39], where they have the remarkable property that their observed brightness at a fixed luminosity is almost independent of redshift over roughly $1 < z < 10$ (Blain & Longair 1993; Blain et al. 2002) due to the shape of their spectral energy distributions (SEDs), an effect which is known as a negative $K$-correction. The technology and instrumentation to exploit this advantage is challenging, however, and ground-based sub-mm/mm instruments have typically only been able to map areas down to depths of a few mJy over hundreds of arcminutes[2] through narrow atmospheric windows (Eales et al. 2000; Scott et al. 2002; Borys et al. 2003; Greve et al. 2004; Laurent et al. 2005; Coppin et al. 2006; Bertoldi et al. 2007; Perera et al. 2008; Scott et al. 2008; Weiß et al. 2009; Austermann et al. 2010; Aretxaga et al. 2011).

Obtaining redshifts for these objects is a painstaking process (see e.g., Chapman et al. 2005). The most common technique up to this point, which relies on identifying the radio or mid-IR counterparts (e.g., Ivison et al. 2007; Roseboom et al. 2010) to provide sufficiently precise localizations and the source being sufficiently bright for successful optical spectroscopy, works relatively poorly at $z > 3$ because such observations do not benefit from negative $K$-corrections. Furthermore, even for very high-$z$ sources, ground-based sub-mm/mm observations are generally limited to probing only the red, Rayleigh-Jeans side of the thermal SED, and hence can only provide extremely crude redshift estimates.

As a result, until recently the number of known $z > 4$ DSFGs was relatively limited, although there were some (mostly photometric) hints that the redshift distribution extended beyond $z = 3$ (e.g. Dannerbauer et al. 2002; Younger et al. 2007, 2009). However, the known $z > 4$ DSFGs were selected in a fairly irregular fashion, making it difficult to place any quantitative limits on the number of such sources. Theoretically, the existence of even the lower-$z$ DSFGs ($z \approx 2.5$) has proven somewhat challenging to explain (e.g., Baugh et al. 2005). The primary challenge is to accrete enough gas into the center of massive dark matter halos at early times in order to fuel these starbursts. These difficulties are only exacerbated at higher redshifts because the number of massive galaxies

is expected to decrease rapidly at high-$z$ (Hayward et al. 2013). Therefore, a significant population of $z > 4$ massive starbursts would be a significant challenge to models. Despite this, there are some indirect lines of evidence that suggest that the most massive galaxies may have formed stars at such early times. In contrast to the bulk of the field galaxy population, for which most star formation occurs after $z = 2$ (e.g., Sobral et al. 2012), studies of the $K$-band luminosity function of clusters show that the stellar mass in the brightest members is already in place earlier (Capozzi et al. 2012). Detailed study of individual sources favors a star formation epoch of $z > 4$ (Stott et al. 2011; Kaviraj et al. 2013). However, what is missing is an effective technique for selecting such sources directly while they are experiencing a starburst.

The *Herschel Space Observatory* (Pilbratt et al. 2010), which observed at multiple bands spanning the peak of the SED at effectively all redshifts, and mapped much larger areas down to the confusion limit than previous surveys, could measure $T_{\rm dust}/(1+z)$ for a large number of individually detected sources. Since most known distant DSFGs have dust temperatures in the range $\sim 20$–$80\,{\rm K}$ (e.g., Kovács et al. 2006; Casey et al. 2012), the observed *Herschel* colors can be used to select potential high-$z$ sources. In this paper we use a map-based technique to search for red, and hence potentially $z > 4$, sources in $21.4\,{\rm deg}^2$ within the Science Demonstration Phase fields from the HerMES[40] project (Oliver et al. 2012) at 250, 350, and $500\,\mu$m. In particular, we select "red" sources with $S_{500\mu m} \geq S_{350\mu m} \geq S_{250\mu m}$ – so-called $500\,\mu$m-risers – to provide a catalog of high-$z$ DSFGs candidates with $S_{500\mu m} \geq 30$ mJy. The highlight of this initial catalog was the discovery of the highest-$z$ massive starburst to date, a $z = 6.34$ source with a star formation rate of $3000\,{\rm M}_\odot {\rm yr}^{-1}$ (FLS 3; Riechers et al. 2013).

We present follow-up of some of these sources, including redshifts for four additional targets from our sample. We find that four of five $500\,\mu$m-risers selected with our technique and with measured redshifts lie at $z > 4$ (and the remaining source is at $z = 3.4$), demonstrating that this technique is an effective method of selecting high-$z$ DSFGs. Returning to the full catalog, we characterize our selection using completeness and purity simulations in order to measure the number density of red sources (§5), show that existing literature models in general significantly under-predict the number of bright, red sources we find (§7.1), and estimate their contribution to the star formation history of the Universe (§7.5). Comparison with other surveys of our fields shows that our sources are redder than typical sources selected at $1\,{\rm mm}$ (§7.2).

## 2. SPIRE OBSERVATIONS AND DATA ANALYSIS

In this paper, we analyze maps of three extragalactic fields observed as part of the HerMES program with the Spectral and Photometric Imaging Receiver (Griffin et al. 2010, SPIRE) on board *Herschel*: *Spitzer* FLS, GOODS North, and the Lockman Hole. The latter has been further subdivided based on mapped depth into the North, East, and SWIRE regions (Table 1). SPIRE observed simultaneously at 250, 350, and $500\,\mu$m. Although the fields were selected based on availability of *Herschel* Science Demonstration Phase (SDP) data, all

University, Ithaca, NY, 14853-6801
[34] Department of Astrophysics, Denys Wilkinson Building, University of Oxford, Keble Road, Oxford OX1 3RH, UK
[35] Infrared Processing and Analysis Center, MS 100-22, California Institute of Technology, JPL, Pasadena, CA 91125
[36] CSIRO Astronomy & Space Science, PO Box 76, Epping, NSW 1710, Australia
[37] Astrophysics Group, Physics Department, University of the Western Cape, Private Bag X17, 7535, Bellville, Cape Town, South Africa
[39] Classic sub-millimeter galaxies (SMGs) are simply DSFGs selected at $\sim 850\,\mu$m.

[40] http://hermes.sussex.ac.uk

available data for these fields, including those beyond the SDP, have been used in the generation of our maps. The basic observation and calibration procedures are described by Griffin et al. (2010); Bendo et al. (2013).

Under the hypothesis that redshift dominates temperature evolution in producing the observed SEDs of distant galaxies, we select objects which have "red" SPIRE colors in the hope of forming a high-redshift sample. This should not be expected to select *all* such sources. For example, the $z = 3$ lensed DSFG LSW 1 (Conley et al. 2011) would not be red in the SPIRE bands unless it were at $z > 7$.

A natural question is why we do not simply search for targets using pre-existing single-band HerMES catalogs by imposing our color and minimum flux density requirements. Catalogs have been produced for these fields in the SPIRE bands which provide a suitable list of $500\,\mu$m sources (Smith et al. 2012; Roseboom et al. 2010). However, at present such catalogs are not optimal for our selection purposes. In many cases, they require detection in the other SPIRE bands or at an alternate wavelength (e.g., $24\,\mu$m) – requirements which will bias against red and therefore, for our purposes, interesting sources. Furthermore, even in those fields where $500\,\mu$m selected catalogs are available, detailed inspection and tests on simulated data show that catalog selection is currently both significantly less pure (i.e., a larger portion of the detected sources are not, in fact, red) and less complete than the map-based method described below.

### 2.1. *Map Construction*

Our map-based search uses products from the SPIRE-HerMES Iterative Map maker (SHIM; Levenson et al. 2010; Viero et al. 2012). Briefly, we use redundant sampling of the same position on the sky with multiple scan directions (cross-scans) to suppress correlated $1/f$ noise via baseline polynomial subtraction and to remove artifacts such as 'glitches' caused by cosmic rays. Our maps are astrometrically aligned with pre-existing radio and *Spitzer*/MIPS $24\,\mu$m data to better than $1''$ accuracy using stacking.

Because SPIRE is diffraction limited, the beam size varies considerably over the three bands from $17.6''$ at $250\,\mu$m to $35.3''$ at $500\,\mu$m (FWHM). In the absence of confusion noise, and for instrument noise that is as white as in the SHIM maps, the mathematically optimum procedure for point-source selection is to smooth the maps by the beam. Since our sources are, by definition, brightest at $500\,\mu$m, we therefore smooth all three maps to an identical resolution of $\sqrt{2} \times 35.3'' = 49.8''$. Since SPIRE maps have significant confusion noise, this approach is not ideal – in the future we plan to improve this procedure by adopting a filtering procedure that takes confusion noise into account, such as that described by Chapin et al. (2011).

In order to facilitate this beam matching, we construct SHIM maps with $4''$ pixels at all bands. This results in incomplete coverage, particularly at $500\,\mu$m (where SPIRE has the lowest sampling density), which is a problem for the convergence of the default SHIM map-maker. However, SHIM makes it possible to re-use baseline and glitch information from maps made at a standard resolution, where convergence is not a problem, and so we have done so for our analysis. We then Gaussian-smooth all the maps to the final resolution, which also fills in the missing coverage due to the small pixels, and then suppress large-scale structure by subtracting a smoothed version of the map (using a smoothing scale of $3'$). Tests on simulated data show that these steps have no significant effect on the accuracy of photometry from the resulting maps, although the smoothing does increase the confusion noise.

### 2.2. *Object Identification in Difference Maps*

Prior to source identification, we form a weighted combination of the SPIRE maps to reduce the confusion from typical, bluer SPIRE galaxies. For simplicity – and because experiments with more complicated (quadratic or cubic) map combinations do not seem to provide better performance – we restrict ourselves to a linear combination. With no loss in generality this can be formulated as:

$$D = k_1 M_{500\,\mu m} + k_2 M_{350\,\mu m} \pm \sqrt{1 - k_1^2 - k_2^2} M_{250\,\mu m}, \tag{1}$$

with $|k_1|$ and $|k_2|$ both $\leq 1$. The term multiplying the $250\,\mu$m map is simply an arbitrary normalization convention, since overall scale factors do not affect our analysis. The sign of this term is another parameter. However – as one would expect, because we are trying to select sources with $S_{500\mu m} \geq S_{250\mu m}$ – the minus sign performs much better, so we adopt it henceforth. Because the maps considered in this paper are confusion-noise dominated, there is little advantage to adopting different $k$ values for the different fields (e.g., applying further noise weighting). We optimized the values of $k_1$ and $k_2$ through simulation, starting with the Béthermin et al. (2011, hereafter B11) model. This model predicts essentially no bright $500\,\mu$m-risers (see §7.1), and so we also include additional red sources in order to evaluate our efficiency at detecting them.

For this purpose we used a preliminary version of the $k$s – which turned out to be very similar to their final values – and injected fake red sources over a range of flux densities and at approximately the observed space density into maps generated from the B11 model, including instrument noise. We then explored a range of values for $k_1$ and $k_2$ by applying the source selection procedure (described in the next section), and used this to estimate the purity (the fraction of detected sources which are red and above our $S_{500\mu m}$ cutoff) and completeness (the fraction of the injected red sources which are recovered) for various values of the $k$'s. Adopting the product of these two factors as our metric, we identified a broad locus of $k_1$, $k_2$ values which provide similar performance.

In order to down-select to the final set of parameters from this set, we further simplified by choosing $k_2 = 0$ and then adopting the value of $k_1$ from the high-performance locus that minimized the variance in the $D$ map for our deepest field (GOODS-N). Our final values are $k_1 = 0.92$, $k_2 = 0.0$. Therefore, for the rest of this analysis, we work with the specific difference map

$$D = 0.920 M_{500\,\mu m} - 0.392 M_{250\,\mu m}. \tag{2}$$

It is somewhat surprising that including the $350\mu$m map in the combination did not improve the performance of the source finding, but this set of parameters performs

**Table 1**
Summary of fields used in this analysis

| Field | RA (deg) | Dec (deg) | Area (deg$^2$) | $\sigma_{250\,\mu m}$ (mJy) | $\sigma_{350\,\mu m}$ (mJy) | $\sigma_{500\,\mu m}$ (mJy) |
|---|---|---|---|---|---|---|
| GOODS-N | 189.23 | 62.22 | 0.33 | 0.8 | 0.8 | 1.0 |
| Lockman-East | 163.14 | 57.49 | 0.34 | 3.6 | 3.6 | 4.0 |
| Lockman-North | 161.49 | 59.01 | 0.46 | 3.6 | 3.5 | 4.1 |
| FLS | 259.05 | 59.29 | 6.83 | 5.1 | 5.3 | 6.5 |
| Lockman-SWIRE | 161.68 | 57.97 | 13.46 | 4.2 | 4.1 | 5.3 |

Note. — Properties of the fields used in this analysis. The RA and Dec are the approximate field centers (J2000), the area excludes regions masked due to the lack of cross-scans. The depths are the approximate $1\sigma$ instrument noise in mJy/beam in the center of each field, not including confusion noise. The Lockman-East and Lockman-North regions are excluded from Lockman-SWIRE. The rms due to confusion in the SPIRE bands is $\sim 6$ mJy/beam (Nguyen et al. 2010).

as well as any other set of parameters in our tests. Any modifications to our procedure (such as changing the applied smoothing, or applying this procedure to shallower, instrument noise dominated maps) are likely to change the optimum values of the $k$s.

We use the measured instrument noise properties of the input SHIM maps to estimate the instrument noise in the difference map ($D$), including the effects of the smoothing, but neglecting the correlations that it imposes between neighboring pixels. We measure the confusion noise in the $D$ maps following the approach of Nguyen et al. (2010), and find a confusion noise of $\sigma_{\rm conf} = 4.2$ mJy. This is less than the confusion noise in the *un*-smoothed single-band SPIRE maps ($\sim 6$ mJy), despite the fact that we have degraded the resolution significantly by smoothing; this, in some sense, is the point of forming the difference map – it effectively removes, or at least de-weights, the bulk of the (non-red) SPIRE-detected population, while reducing the signal from red sources by considerably less. Note that the slope of the mean relation between $S_{500\mu m}$ and $S_{250\mu m}$ map pixels is $\sim 2.3$ (Figure 1). The fact that this is so close to the ratio of our coefficients (2.36), which were derived from a process that also included considerations related to red source recovery, is encouraging.

The noise in areas of the maps without cross scans is more complicated and difficult to simulate. Therefore, we masked the edges of our maps to exclude such regions as well as to provide better uniformity in sampling density. We then search for sources in the difference map using StarFINDER[41] (Diolaiti et al. 2000), a package designed for source detection in crowded fields. Because the instrument noise estimate ignores the correlations induced by the smoothing procedure, and because the confusion noise distribution is highly non-Gaussian, it is important to use simulations to select the minimum signal-to-noise (S/N) requirement to impose on the source finding in order to optimize the purity and completeness of the resulting catalog. Based on such simulations (see §5.4), we have adopted a minimum S/N of 4, where the noise is the quadrature sum of the $1\sigma$ instrument and confusion noise. Because our fields range considerably in depth, the S/N requirement translates to different limits in $D$ for different fields. For the large, shallow fields that dominate our catalog, $D > 25.0$ mJy in FLS, and $D > 23.4$ mJy in Lockman-SWIRE. The depths for the smaller, deeper fields are $D > 19.4$ mJy in Lockman-North and Lockman-East, and $D > 17.3$ mJy

[41] http://www.bo.astro.it/StarFinder/paper6.htm

in GOODS-N.

### 2.3. Selection of Sources Rising at 500 μm

The choice $k_1 = 0.92, k_2 = 0$ in the difference images allows "leakage" of bright sources which are somewhat blue ($1 < S_{250\mu m}/S_{500\mu m} < 2.3$). Selecting only sources which rise in $500\,\mu m$ band thus requires an additional selection step. At the position of each detected source in the difference maps, we measure the three SPIRE flux densities from the smoothed maps, since, given our typical positional uncertainties (§4.3), measuring the flux densities from the un-smoothed maps results in significant biases. We use these measurements to further impose the requirements $S_{500\mu m} \geq S_{350\mu m} \geq S_{250\mu m}$ and $S_{500\mu m} \geq 30$ mJy, the effects of which are shown in Figure 1. The last criterion selects sources which are bright enough for relatively easy follow-up. Furthermore, sources fainter than this limit generally have very low detection efficiencies in the SPIRE data using our method (typically 5–20%), and the uncertainties in those efficiencies are quite large because we do not know their flux densities precisely. Therefore, if we were to include sources below this limit, it would significantly degrade the precision of our source density measurement (see §5).

Once sources are identified from the difference maps, we match our targets against the HerMES SCAT catalogs (Smith et al. 2012), which are based on the un-smoothed maps, and provide more precise flux measurements; recall that the reason for not using the catalogs to select red targets is because a catalog search results in a larger number of false sources, but once red targets are identified by the map search this concern no longer applies. This is not possible in all cases, because some of our red sources were not detected by SCAT, possibly because they are too faint in the bluer (250 and $350\,\mu m$) SPIRE bands. We use the SCAT v21 catalogs selected at $350\,\mu m$ for this purpose – the 250 and $500\,\mu m$ selected catalogs (where available) are generally too incomplete for red sources for our purposes.

In addition, we have visually inspected all sources which pass these cuts in order to remove (rare) noise artifacts, and to note blends of faint sources. The more difficult cases involve noise artifacts on top of real sources which cause them to appear red. However, in general, such false sources are quite easy to detect in the un-smoothed maps, and have been removed from our analysis. In §5.2 we make use of simulations to quantify the effects of instrument noise scattering "orange" sources across the selection boundary.

The 38 sources which meet all selection criteria are
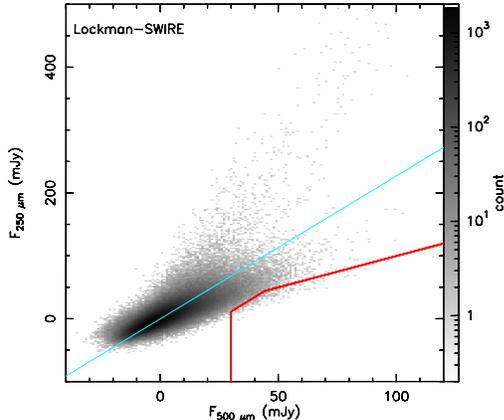
**Figure 1.** Two-dimensional histogram illustrating the difference map selection used in this paper. The axes are SPIRE $500\,\mu m$ and $250\,\mu m$ map-based flux densities. The grayscale gives the number of counts in each flux-flux bin for the Lockman-SWIRE field. The cyan line shows the "average" color of the galaxies, based on minimizing the variance in the difference image $D(k_1)$. The red line segments show the boundary for object selection, a combination of the threshold in $D$, the requirement $S_{500\mu m} \geq S_{250\mu m}$, and the $S_{500\mu m} \geq 30$ mJy requirement. The further selection criteria $S_{500\mu m} \geq S_{350\mu m}$ and $S_{350\mu m} \geq S_{250\mu m}$ are not illustrated here. The input data are the oversampled images; a single galaxy occupies multiple pixels and hence multiple bins. This potential redundancy in object selection is eliminated by the peak finding algorithm. Note that the maps have zero mean before and after point-source filtering, and the bins with significant negative flux densities represent pixels between objects.

listed in Table 2 and form the basic sample for this paper. There is one in GOODS-N, 18 in FLS, and 19 in the combined Lockman regions. In addition we include in the table two bright sources (LSW 28 and LSW 102) from outside our field mask (due to the lack of cross-scans at their positions), but do not include them in our formal catalog. Both sources easily pass our selection criteria, and are clearly real; in fact the redshift of LSW 102 is 5.3 (Perez-Fournon et al. , in preparation). LSW 28 is a few arcminutes away from the 2nd magnitude star $\beta$ Ursa Major, which causes complications for optical/near-IR follow-up. For comparison, we also include in the table (but not in the statistical analysis) the known $z = 4$ source pair GN20/20.2 (Pope et al. 2005; Daddi et al. 2009); it barely fails our selection criteria. Note that this pair has a separation of $24''$, and hence is resolved in the $250\mu m$ channel. The quoted SCAT and radio fluxes are the sum of both. The positions in Table 2, and throughout this paper, are the centroids in the difference $(D)$ images and have $\sim 5''\ 1\sigma$ uncertainty (see §4.3). Sources identified as blends or which do not satisfy $S_{500\mu m} \geq S_{350\mu m}$ are identified in the table. For comparison, the SCAT catalogs of these fields contain $\sim 1400$ non-red sources with $S_{500\mu m} > 30$ mJy. Based on their flux densities, pre-existing lensing models for the DSFG population predict that most of our sources should not be significantly lensed (e.g., Negrello et al. 2007; Wardlow et al. 2013). However, these models were developed for lower-$z$ DS-FGs, so this will have to be tested against future interferometric observations. Cutouts of all of the sources in our final catalog are shown in Figures 2 and 3.

### 2.4. Screening against Synchrotron Sources

Since bright synchrotron-emitting galaxies may have far-IR spectra consistent with our selection criteria at

modest ($\leq$ 1) redshifts, we screen against such objects by searching for bright ($>1$ mJy) radio counterparts. We used the NVSS and FIRST 21 cm catalogs (Becker, White, & Helfand 1995; Condon et al. 1998), which cover our fields, and found one such radio-bright source coincident with a SPIRE source in our sample: LSW 25. This turns out to be a known BL Lac at a redshift of $z = 0.83$ (Richards et al. 2009), and we exclude it from all further analysis. Another SPIRE source, LSW 48, lies $21''$ away from a radio source with a 21 cm flux density of 2.8 mJy; given the typical positional accuracy, this is unlikely to be due to the same source, so we retain LSW 48 in our sample. FLS 3 and GOODSN 8 have significantly deeper 21 cm observations (see §4.4). For the remaining sources we provide the catalog detection limit at that position in Table 2. Four more of our targets are covered by deeper, narrower observations at 19–20 cm, which are presented in §4.4. Other than LSW 25, the radio flux densities of all our sources are faint enough to be consistent with the FIR/radio correlation seen for star-forming galaxies at $z \simeq 4$ (Ivison et al. 2010), implying that they are dust-emission dominated.

### 3. BASIC OBSERVED FAR-IR SOURCE PROPERTIES

For each source, we fit a modified blackbody spectrum to the three SPIRE flux densities, with the primary goal of determining the wavelength at which the spectrum reaches its maximum. This information is used to estimate the redshift distribution of the population in §7.4. Given the small number of SPIRE bands, it is not possible to fully constrain such a model. In such cases it is common in the literature to assume that the emission is optically thin and furthermore to fix the log-slope $\beta$ of the optical depth curve to some nominal value ($\approx 1.5$): $S_\nu (\lambda_{\rm obs}) \propto \lambda_{obs}^{-\beta} B_\nu (T_{\rm d}/(1+z))$, where $B_\nu$ is the Planck function, $T_{\rm d}$ the dust temperature, and $\lambda_{\rm obs}$ the observer frame wavelength. (Note that, as is common in sub-mm/mm astronomy, we work in $S_\nu$ units but expressed as a function of wavelength.)

In this paper we instead use the slightly more general formalism of an optically-thick modified blackbody:

$$S_\nu (\lambda_{\rm obs}) = \Omega \ \times \ \left(1 - \exp\left[-(\lambda_0 (1+z)/\lambda)^\beta\right]\right) \times$$
$$B_\nu (\lambda_{\rm obs}; T_{\rm d}/(1+z)), \qquad (3)$$

where $\lambda_0$ is the (rest-frame) wavelength where the optical depth reaches unity and $\Omega$ is the solid angle subtended by the source. To the blue side of this relation we attach a power law $S_\nu \propto \lambda^\alpha$, joining the two by requiring the SED and first derivative to be continuous. We fit this model to the data using an affine-invariant Markov Chain Monte-Carlo (MCMC) approach, as discussed in the Appendix. In the current section, where we only analyze SPIRE photometry, we marginalize over broad priors in the less well constrained model parameters rather than fixing them. Later, for sources where more photometry is available (§4.7) we remove these priors. In all cases in this paper, $\alpha$ is poorly constrained, with the fits only providing a lower limit. Because of the way the blue-side power law is joined to the modified blackbody portion of the SED (requiring that the first derivatives match), this simply amounts to a statement that the merge point between the power law and the

**Table 2**
SPIRE and radio fluxes for sources selected as described in Section 2.3.

| Source Name | Position | | Smoothed Map | | | | SCAT | | | Radio |
|---|---|---|---|---|---|---|---|---|---|---|
| | $\alpha_{2000}$ (deg) | $\delta_{2000}$ (degrees) | $S_{250\,\mu m}$ (mJy) | $S_{350\,\mu m}$ (mJy) | $S_{500\,\mu m}$ (mJy) | $D$ (mJy) | $S_{250\,\mu m}$ (mJy) | $S_{350\,\mu m}$ (mJy) | $S_{500\,\mu m}$ (mJy) | $S_{21\,cm}$ ($\mu$Jy) |
| GOODSN 8[x] | 188.964 | 62.363 | 22.7 | 33.6 | 35.9 | 20.9 | $\cdots$ | $\cdots$ | $\cdots$ | $27 \pm 4$ (§4.4) |
| FLS 1 | 257.072 | 58.479 | 50.7 | 82.9 | 87.4 | 61.6 | 62.3 | 94.0 | 98.2 | $< 840$ |
| FLS 3 | 256.697 | 58.772 | 13.4 | 26.8 | 47.5 | 37.9 | 12.0 | 32.4 | 47.3 | $59 \pm 11$ |
| FLS 5 | 260.204 | 59.773 | 17.1 | 40.0 | 47.7 | 37.3 | 24.7 | 45.1 | 48.2 | $< 920$ |
| FLS 6 | 256.797 | 60.470 | 39.3 | 53.0 | 53.7 | 26.6 | $\cdots$ | $\cdots$ | $\cdots$ | $< 1200$ |
| FLS 7[b,x] | 257.511 | 59.089 | 24.2 | 50.2 | 51.7 | 40.4 | $\cdots$ | $\cdots$ | $\cdots$ | $< 1030$ |
| FLS 17 | 260.794 | 60.331 | 33.7 | 43.0 | 48.7 | 27.7 | 28.4 | 42.5 | 48.6 | $< 960$ |
| FLS 19 | 258.754 | 60.429 | 11.5 | 21.9 | 36.9 | 27.2 | 15.0 | 21.2 | 31.4 | $< 980$ |
| FLS 20 | 256.407 | 60.370 | 29.9 | 39.5 | 50.8 | 36.4 | 25.1 | 34.7 | 43.5 | $< 1080$ |
| FLS 22 | 257.863 | 60.632 | 2.5 | 31.9 | 40.0 | 34.3 | 14.5 | 33.2 | 37.1 | $< 1010$ |
| FLS 23[b] | 260.334 | 58.571 | 29.6 | 39.6 | 41.6 | 32.9 | 12.3 | 26.7 | 31.7 | $< 1010$ |
| FLS 24 | 261.196 | 59.556 | 2.0 | 26.1 | 32.6 | 31.7 | 16.3 | 32.2 | 34.3 | $< 960$ |
| FLS 25 | 259.788 | 60.121 | 29.6 | 41.2 | 45.6 | 32.6 | 31.6 | 40.3 | 42.9 | $< 1020$ |
| FLS 26[x] | 257.798 | 58.963 | 15.8 | 30.8 | 35.0 | 30.8 | $\cdots$ | $\cdots$ | $\cdots$ | $< 980$ |
| FLS 30[x] | 258.364 | 58.401 | 47.5 | 52.3 | 54.7 | 29.7 | $\cdots$ | $\cdots$ | $\cdots$ | $< 910$ |
| FLS 31[x] | 257.644 | 58.639 | $-2.0$ | 26.4 | 33.0 | 27.6 | $\cdots$ | $\cdots$ | $\cdots$ | $< 990$ |
| FLS 32[x] | 261.148 | 60.053 | 10.9 | 20.6 | 34.2 | 26.4 | $\cdots$ | $\cdots$ | $\cdots$ | $< 1000$ |
| FLS 33 | 259.879 | 60.475 | 26.3 | 42.1 | 44.3 | 26.9 | 21.6 | 39.6 | 40.6 | $< 1010$ |
| FLS 34[x] | 257.110 | 59.680 | 16.7 | 33.7 | 40.7 | 27.8 | 16.7 | 33.7 | 40.7 | $< 950$ |
| LSW 20 | 162.885 | 56.605 | 4.5 | 21.5 | 39.0 | 33.1 | 17.6 | 36.6 | 43.9 | $< 920$ |
| LSW 25[r] | 159.435 | 57.198 | 47.5 | 59.9 | 64.3 | 41.6 | 51.3 | 66.9 | 69.7 | 127,000 |
| LSW 26[y] | 161.056 | 58.770 | 13.4 | 30.3 | 31.4 | 27.4 | 23.9 | 39.0 | 34.2 | $< 980$ |
| LSW 29 | 161.935 | 57.942 | 30.1 | 50.0 | 51.2 | 31.5 | 32.5 | 47.5 | 50.3 | $< 980$ |
| LSW 31[x] | 160.973 | 59.361 | 40.6 | 53.8 | 57.2 | 39.8 | $\cdots$ | $\cdots$ | $\cdots$ | $< 970$ |
| LSW 47[x] | 162.148 | 57.936 | 29.0 | 52.5 | 53.5 | 38.7 | $\cdots$ | $\cdots$ | $\cdots$ | $< 960$ |
| LSW 48[y] | 163.427 | 56.590 | 3.4 | 22.1 | 29.8 | 34.1 | 22.6 | 41.7 | 40.9 | $< 950$ |
| LSW 49 | 159.652 | 57.698 | 27.2 | 44.4 | 48.1 | 33.9 | 23.1 | 38.5 | 40.1 | $< 1040$ |
| LSW 50[x] | 163.274 | 56.684 | $-2.1$ | 18.0 | 30.3 | 32.7 | $\cdots$ | $\cdots$ | $\cdots$ | $< 950$ |
| LSW 52 | 163.954 | 57.566 | 17.3 | 32.6 | 43.7 | 31.6 | 16.3 | 33.0 | 40.2 | $< 990$ |
| LSW 53 | 163.135 | 58.607 | 31.5 | 40.7 | 44.9 | 31.9 | 15.8 | 29.7 | 32.6 | $< 1030$ |
| LSW 54 | 163.743 | 57.061 | 31.9 | 41.0 | 44.0 | 30.9 | 36.6 | 46.0 | 46.7 | $< 920$ |
| LSW 55[x] | 164.774 | 57.751 | 7.7 | 24.7 | 31.2 | 29.2 | $\cdots$ | $\cdots$ | $\cdots$ | $< 970$ |
| LSW 56 | 165.086 | 58.028 | 23.6 | 41.1 | 43.3 | 29.5 | 28.4 | 41.7 | 44.8 | $< 1020$ |
| LSW 58 | 163.391 | 56.608 | 7.2 | 28.8 | 32.3 | 27.8 | 15.6 | 29.5 | 34.1 | $< 950$ |
| LSW 60[x] | 161.914 | 60.087 | 28.6 | 47.3 | 47.6 | 32.9 | $\cdots$ | $\cdots$ | $\cdots$ | $< 1210$ |
| LSW 76[x] | 165.353 | 59.063 | 41.1 | 60.1 | 61.3 | 40.4 | $\cdots$ | $\cdots$ | $\cdots$ | $< 1030$ |
| LSW 81[y] | 163.649 | 56.522 | 20.2 | 38.7 | 41.4 | 26.6 | 29.6 | 45.0 | 43.1 | $< 1010$ |
| LSW 82 | 165.420 | 58.227 | 21.9 | 33.4 | 37.5 | 25.9 | 16.4 | 34.7 | 37.2 | $< 920$ |
| LSW 28[c] | 165.366 | 56.326 | 35.1 | 53.6 | 64.0 | 45.2 | 33.4 | 55.9 | 60.0 | $< 960$ |
| LSW 102[c] | 160.211 | 56.115 | 51.0 | 122.3 | 140.0 | 109.4 | 49.7 | 118.1 | 140.4 | $< 1010$ |
| GN20/20.2[b,o] | 189.300 | 62.370 | 52.3 | 68.6 | 65.4 | 38.2 | 59.4 | 75.2 | 74.1 | $289 \pm 13$ |

[b] Source is clearly detected as blended in un-smoothed 250 $\mu$m maps.
[c] Source is in a region of the maps that does not have redundant scans, and hence not included in the statistical analysis.
[o] Known $z = 4$ source not detected by our pipeline, but included for comparison.
[r] Radio-loud object dominated by synchrotron emission; omitted from sample.
[x] Source not present in SCAT v21 350 $\mu$m selected catalog.
[y] Source with $S_{350\mu m} > S_{500\mu m}$ in the SCAT catalog.

**Note.** — SPIRE and radio parameters for sources detected via our map-based method. The first three 250/350/500 $\mu$m flux densities are those derived from the smoothed maps, and $D$ is the flux density measured in the linear map combination described in the text. The SCAT-derived SPIRE flux densities are measured from the un-smoothed maps at the native SPIRE resolution, and are from the SCAT v21 HerMES catalogs. The typical instrumental noise uncertainty in both sets of SPIRE flux densities is 2–3 mJy. The calibration uncertainties for SPIRE are about 5%, and the confusion noise is $\sim$ 6 mJy in the un-smoothed maps; note, however, that both are highly correlated between bands, so have a minor effect on the color ratios between SPIRE bands. The SCAT flux densities, where available, are expected to be more accurate. The $\sim$ 1000 $\mu$Jy 21 cm flux density upper limits are from the FIRST or NVSS catalogs. For brighter sources, the positional accuracy is $\sim 5''$ (see §4.3). The names of these sources are drawn from a master list that includes additional, non-red HerMES sources.

thermal SED lies at wavelengths lower than the shortest wavelength photometry point (250 $\mu$m). That is, in all cases, the quality of our fits is not improved by the addition of the Wien-side power law, and, while formally included, $\alpha$ is effectively not a parameter of our fits.

Due to the poor constraints possible with only SPIRE data, we marginalize over broad Gaussian priors in $\beta$ and $\lambda_0 (1 + z)$. There is relatively little guidance in the literature for the appropriate value for $\lambda_0$, although 100 $\mu$m has been adopted in some studies. In general, both *Her-*
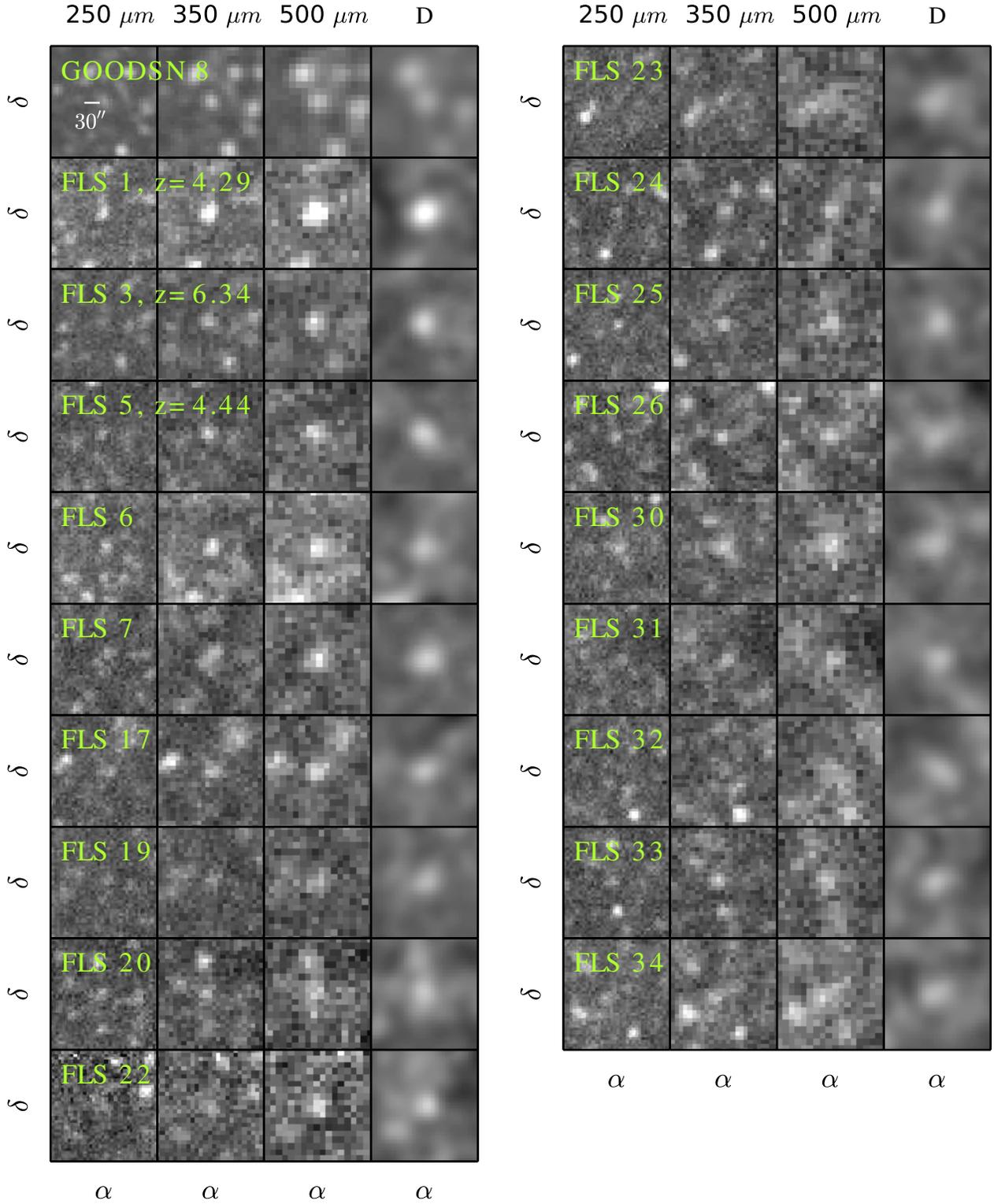
**Figure 2.** Postage stamps of all of the GOODS-N and FLS sources in our catalog. The grayscale range for each cutout is -35 to +50 mJy. Sources with secure spectroscopic redshifts are noted. For explanation of the 'D' image, see §2.2.

*schel* and longer $\lambda$ observations are required to constrain $\lambda_0$, and hence it has been measured for relatively few sources. In order to determine an appropriate prior, we

have applied this same model to literature sources with a sufficient quantity of high quality photometry such as Arp 220 (Rangwala et al. 2011), LSW 1 (Conley et al.
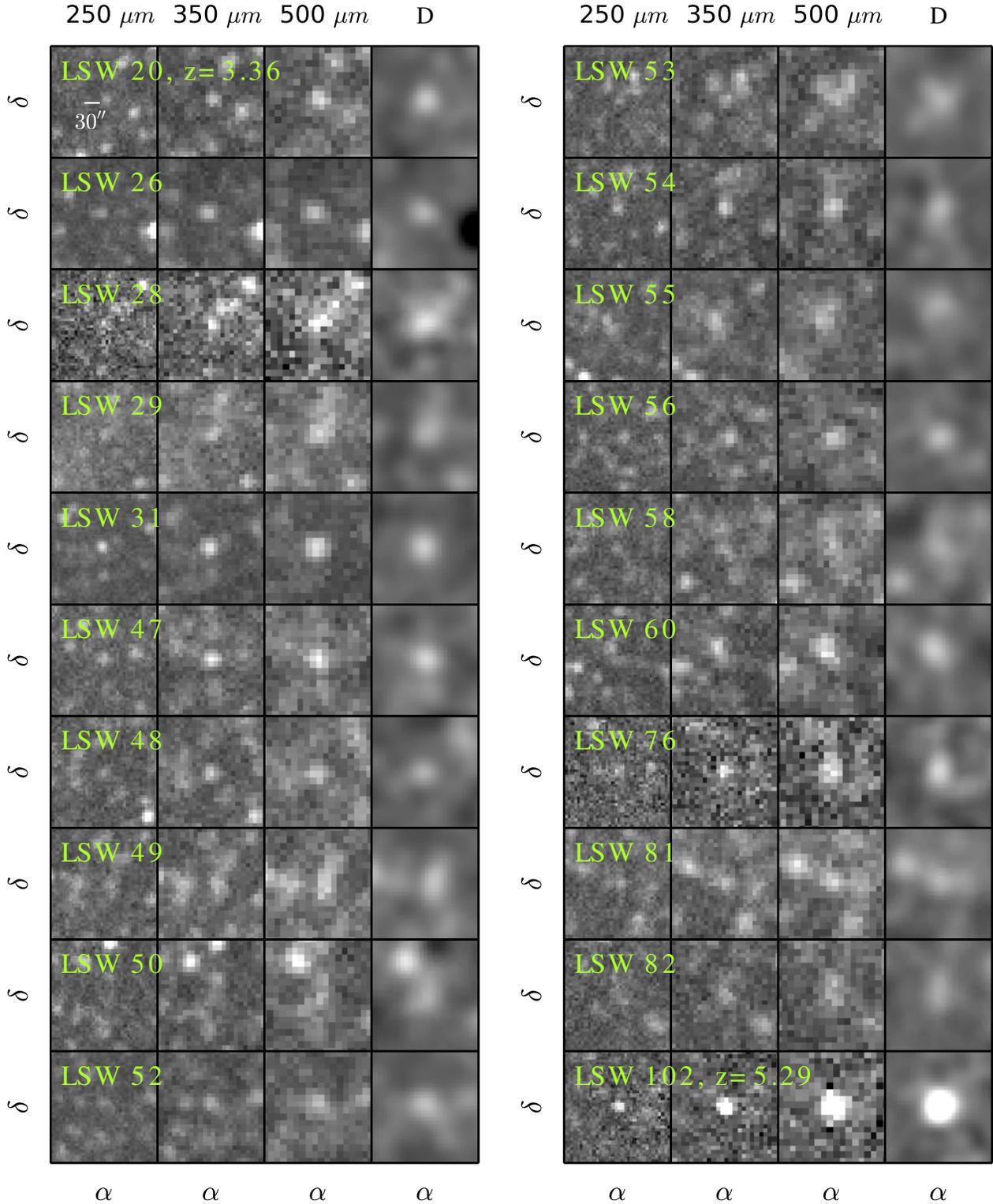
**Figure 3.** Postage stamps of all of the LSW sources in our catalog. The grayscale range for each cutout is -35 to +50 mJy. Sources with Sources with secure spectroscopic redshifts are noted. For explanation of the 'D' image, see §2.2.

2011), the Cosmic Eyelash (Swinbank et al. 2010), FLS 3 (Riechers et al. 2013), XMM 1 (Fu et al. 2013), ID 141 (Cox et al. 2011), as well as three of the red sources pre-

sented in this paper (§4.7). We conclude that, with the exception of FLS 3, all sources are significantly better fit by an optically thick model rather than an optically thin

one, with $\Delta\chi^2$ values of $> 6$, and that $\lambda_0$ ranges from 190 to 270 $\mu$m (rest frame). If our sources have a typical redshift of $4.5 \pm 1$, this corresponds to a Gaussian prior on $\lambda_0\,(1+z)$ of $1100 \pm 400\,\mu$m, which we adopt (truncating the prior to exclude negative values). We further assume a Gaussian prior on $\beta$ of $1.8 \pm 0.3$ (Draine 2006). $\beta$ is typically believed to be below 2, but examples of larger values are known (e.g., Schwartz 1982), so we do not set a hard upper limit in our analysis.

We use the SCAT v21 catalog flux densities where available, and otherwise the smoothed map fluxes (Table 2). In addition to the instrumental uncertainties in the catalog fluxes (typically 2–3 mJy), we include 4% grayscale calibration uncertainty, a 1.5% per-band uncorrelated calibration uncertainty (Bendo et al. 2013), and confusion noise due to the modest SPIRE resolution. We estimate the covariance matrix of the latter using simulations based on the B11 model, (slightly) scaled to match the observed confusion noise (Nguyen et al. 2010). Note that we use a different confusion noise covariance matrix for fluxes derived from the un-smoothed and smoothed maps (SCAT vs. map based) – in the latter case the confusion noise is larger. However, in either case, as the confusion noise and calibration uncertainties are highly correlated among the bands, they have relatively little effect on estimates of the peak wavelength and temperature. It is clear that longer-wavelength observations ($\lambda = 750$–$2000\,\mu$m) would significantly improve our SED constraints.

The fit results are given in Table 3. For most of our sources, the SPIRE data are well fit by a single temperature modified blackbody, with the possible exception of FLS 31. Histograms of $T_{\rm d}/\,(1+z)$ and $\lambda_{\rm max}$ (the observer frame peak wavelength of $S_\nu$ estimated from our SED fits)[42] are shown in Figure 4. These central values are relatively insensitive to the exact form of the priors, although $\lambda_{max}$ is less sensitive than $T_{\rm d}/\,(1+z)$. For example, if we change the $\beta$ prior to $1.5 \pm 0.3$, $\lambda_{\rm max}$ changes by $< 1\%$ and $T_{\rm d}/\,(1+z)$ increases by about 5%. $L_{\rm IR}$, however, is fairly sensitive to the $\beta$ prior (in the absence of additional photometry and assuming a fixed $z$). The results are even less sensitive to the $\lambda_0$ prior, particularly $\lambda_{\rm max}$, although if we adopt an optically-thin model ($\lambda_0 \to 0$), $T_{\rm d}/\,(1+z)$ drops by about 15%.

FLS 3 ($z = 6.3$) is one of the reddest sources, but there are others as red in our sample. Some of the sources have mm-wave follow-up (see §4). We can use this to check whether our priors were reasonable by using our model to predict these flux densities and comparing them with observations, and by comparing the predicted $\lambda_{\rm max}$ from SPIRE data to that measured when the peak is better constrained by adding mm-data. With the exception of FLS 17, which is significantly fainter than predicted at 1.3mm, we find that this model does a good job predicting the mm-fluxes and $\lambda_{\rm max}$, albeit with large (10-25%) uncertainties. For example, for FLS 5 $\lambda_{\rm max}$ (SPIRE) $= 452 \pm 37\,\mu$m, while the value measured with the addition of mm data is $445 \pm 20\,\mu$m. For FLS 3 the values are $550 \pm 86\,\mu$m and $537 \pm 22\,\mu$m; the modest improvement in the precision on $\lambda_{\rm max}$ when mm-data are added is because of the additional priors applied to the

---

[42] Note that in an optically thick modified blackbody model $\lambda_{\rm max} \not\propto (1+z)\,/T_{\rm d}$, even if all other parameters are fixed.
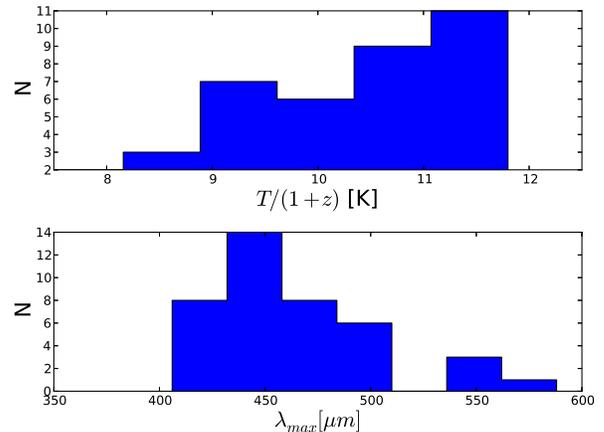


**Figure 4.** Results of the modified blackbody fits to the SPIRE photometry of our sources. The top panel shows the measured $T_{\rm d}/\,(1+z)$ distribution, and the bottom panel the observer-frame wavelength at which $S_\nu$ peaks.

SPIRE-only fits.

## 4. FOLLOW-UP OBSERVATIONS

We are carrying out a multi-wavelength follow-up program of these sources. By design, the SPIRE data only sample the blue side of the thermal SED well, and so longer-wavelength sub-mm/mm observations are particularly critical. They are used to determine whether our sources do, in fact have thermal SEDs, and constrain their total IR luminosity, dust mass, etc. In addition, mm-wave line searches can be used to measure redshifts and model molecular gas excitation properties, and high-resolution interferometric observations can be used to identify counterparts at other wavelengths and to study source morphologies (e.g., Riechers et al. 2013).

In this section we describe the relevant observations of the targets for this paper (Table 4), concentrating on the mm-band and radio continuum flux densities and redshifts. Other details, such as precise positions, morphologies, and line ratios, will be presented elsewhere. Four of our sources (FLS 1, FLS 3, FLS 5, and LSW 20) have sub-mm/mm observations and known redshifts from PdBI, SMA, Z-Spec, and CARMA, as described below. FLS 3 ($z = 6.34$) has particularly extensive follow-up, which is described elsewhere (Riechers et al. 2013). How the sources with redshifts relate to the rest of the catalog sources presented here, as well as to 500 $\mu$m-risers selected from the literature by other means, is shown in Figure 5.

### 4.1. Pre-existing Multi-wavelength Observations

All of the HerMES fields have deep ancillary data partially covering the SPIRE maps, and the majority of our sources have *Spitzer* observations from 3.5 to 160$\mu$m. However, counterpart identification is found to be challenging for our galaxy sample due to the relatively large SPIRE beam, the expected faintness of our sources at other wavelengths compared with the depth of the available observations, and the large number of potential counterparts in the 3.5-8$\mu$m bands. While it would be tempting to simply assume that the brightest or closest *Spitzer* 24 $\mu$m source in the vicinity of each candidate, if there is one, is the correct match, it is difficult to justify

**Table 3**
Quantities derived from the SPIRE observations

| Source | $T_{\rm d}/(1+z)$ (K) | $\lambda_{\max}$ ($\mu$m) | $L_{\rm IR}\,(z=4.7)^a$ ($10^{12}\,{\rm L_\odot}$) | $\chi^2$ | $\epsilon^b$ |
|---|---|---|---|---|---|
| GOODSN 8 | $11.3 \pm 3.0$ | $433 \pm 83$ | $37 \pm 20$ | 0.08 | $0.51 \pm 0.17$ |
| FLS 1 | $10.8 \pm 0.8$ | $440 \pm 21$ | §4.7 | 0.02 | $0.68 \pm 0.08$ |
| FLS 3 | $8.1 \pm 1.2$ | $550 \pm 56$ | Riechers et al. (2013) | 0.02 | $0.88 \pm 0.04$ |
| FLS 5 | $10.3 \pm 1.2$ | $452 \pm 37$ | §4.7 | 0.12 | $0.57 \pm 0.08$ |
| FLS 6 | $11.4 \pm 2.6$ | $423 \pm 68$ | $57 \pm 26$ | 0.09 | $0.57 \pm 0.12$ |
| FLS 17 | $9.9 \pm 1.9$ | $466 \pm 50$ | $40 \pm 15$ | 0.05 | $0.63 \pm 0.13$ |
| FLS 19 | $7.2 \pm 3.3$ | $558 \pm 117$ | $24^{+14}_{-11}$ | 0.05 | $0.62 \pm 0.15$ |
| FLS 20 | $8.3 \pm 3.5$ | $507 \pm 87$ | $44^{+25}_{-21}$ | 0.08 | $0.58 \pm 0.18$ |
| FLS 22 | $9.6 \pm 1.4$ | $479 \pm 49$ | $24 \pm 7$ | 0.45 | $0.50 \pm 0.18$ |
| FLS 24 | $9.9 \pm 1.6$ | $463 \pm 53$ | $24 \pm 7$ | 0.21 | $0.51 \pm 0.17$ |
| FLS 25 | $10.6 \pm 3.0$ | $436 \pm 60$ | $50^{+31}_{-23}$ | 0.15 | $0.34 \pm 0.11$ |
| FLS 26 | $11.1 \pm 2.6$ | $437 \pm 75$ | $37 \pm 18$ | 0.02 | $0.47 \pm 0.13$ |
| FLS 30 | $9.6 \pm 3.8$ | $475 \pm 108$ | $69^{+54}_{-42}$ | 0.11 | $0.48 \pm 0.15$ |
| FLS 31 | $10.7 \pm 2.3$ | $442 \pm 68$ | $30^{+11}_{-13}$ | 1.88 | $0.56 \pm 0.13$ |
| FLS 32 | $6.7 \pm 3.0$ | $588 \pm 122$ | $28 \pm 13$ | 0.07 | $0.52 \pm 0.12$ |
| FLS 33 | $10.5 \pm 1.0$ | $444 \pm 43$ | $34 \pm 9$ | 0.01 | $0.43 \pm 0.13$ |
| FLS 34 | $9.2 \pm 1.5$ | $494 \pm 55$ | $26 \pm 8$ | 0.02 | $0.60 \pm 0.09$ |
| LSW 20 | $9.3 \pm 1.3$ | $490 \pm 49$ | §4.7 | 0.03 | $0.68 \pm 0.08$ |
| LSW 26 | $11.5 \pm 1.7$ | $406 \pm 40$ | $30^{+7}_{-10}$ | 0.64 | $0.38 \pm 0.12$ |
| LSW 29 | $11.1 \pm 1.4$ | $432 \pm 37$ | $43 \pm 13$ | 0.12 | $0.59 \pm 0.09$ |
| LSW 31 | $10.6 \pm 2.5$ | $450 \pm 73$ | $57 \pm 28$ | 0.04 | $0.61 \pm 0.09$ |
| LSW 47 | $11.6 \pm 2.0$ | $412 \pm 50$ | $49^{+15}_{-19}$ | 0.21 | $0.53 \pm 0.12$ |
| LSW 48 | $10.7 \pm 1.4$ | $434 \pm 38$ | $31 \pm 8$ | 0.53 | $0.37 \pm 0.09$ |
| LSW 49 | $10.6 \pm 1.1$ | $440 \pm 43$ | $32 \pm 10$ | 0.02 | $0.45 \pm 0.15$ |
| LSW 50 | $8.1 \pm 2.5$ | $541 \pm 102$ | $26^{+8}_{-11}$ | 0.34 | $0.58 \pm 0.11$ |
| LSW 52 | $9.1 \pm 1.5$ | $495 \pm 54$ | $25 \pm 6$ | 0.02 | $0.59 \pm 0.09$ |
| LSW 53 | $9.7 \pm 1.8$ | $470 \pm 59$ | $23^{+6}_{-8}$ | 0.05 | $0.27 \pm 0.13$ |
| LSW 54 | $11.4 \pm 2.2$ | $413 \pm 44$ | $55^{+30}_{-22}$ | 0.16 | $0.46 \pm 0.14$ |
| LSW 55 | $10.3 \pm 3.0$ | $455 \pm 90$ | $32 \pm 15$ | 0.17 | $0.46 \pm 0.07$ |
| LSW 56 | $10.5 \pm 1.8$ | $443 \pm 46$ | $40 \pm 14$ | 0.06 | $0.62 \pm 0.04$ |
| LSW 58 | $9.5 \pm 1.8$ | $483 \pm 63$ | $24 \pm 7$ | 0.01 | $0.45 \pm 0.17$ |
| LSW 60 | $11.8 \pm 2.3$ | $410 \pm 59$ | $48^{+18}_{-21}$ | 0.05 | $0.52 \pm 0.14$ |
| LSW 76 | $11.5 \pm 2.1$ | $421 \pm 54$ | $56^{+17}_{-22}$ | 0.04 | $0.57 \pm 0.12$ |
| LSW 81 | $11.4 \pm 1.6$ | $414 \pm 35$ | $39 \pm 13$ | 0.06 | $0.42 \pm 0.10$ |
| LSW 82 | $9.8 \pm 1.4$ | $471 \pm 51$ | $26 \pm 7$ | 0.43 | $0.40 \pm 0.08$ |
| LSW 28 | $10.5 \pm 1.1$ | $448 \pm 32$ | $42 \pm 9$ | 0.02 | $\cdots$ |
| LSW 102 | $8.7 \pm 0.8$ | $476 \pm 18$ | $75 \pm 9$ | 1.02 | $\cdots$ |

$^a$Inferred 8–1000 $\mu$m (rest frame) infrared luminosity, assuming $z = 4.7$ (§7.4). These values assume no lensing.
$^b$Selection efficiency (see §5.1).

**Note**. — The dust temperature, wavelength at which $S_\nu$ peaks (observer frame), $L_{IR}$, and $\chi^2$ values are from modified blackbody fits to the SPIRE photometry of our sources, as detailed in §3. The effective number of degrees of freedom for the $\chi^2$ values is one. The uncertainties are the 68.3% confidence limits, which are quite non-Gaussian for some sources. Known blended sources (FLS 7 and FLS 23) are not included because their intrinsic flux densities are not known.

– or check – this assumption without additional data. Therefore, we postpone discussion of the near- and mid-IR counterparts of our sources for a later publication, by which time the number of sources with precise interferometric positions will have increased.

### 4.2. *Single-dish mm Observations: Z-Spec and Bolocam*

Four of the sources in our final catalog were observed with Z-Spec on the Caltech Submillimeter Observatory (CSO) in 2010 March-May during favorable conditions ($\tau_{225\,\rm GHz}$(zenith) = 0.05 – 0.11): FLS 1, FLS 3, FLS 5, and LSW 20. Z-Spec is an $R \approx 250$ grating spectrometer covering the full spectral range from $\lambda = 0.97$ to $1.58$ mm (Earle et al. 2006), with a beam FWHM ranging from 25 to 33″ over the band. All of the sources were detected, with 1.1 mm continuum flux densities of 10–30 mJy. The

spectra for FLS 1, FLS 3, FLS 5, and LSW 20 are shown in Figure 6 and Table 4. We performed a search for lines in these spectra using the redshift search algorithm detailed in Lupu et al. (2012), but did not detect any features at greater than $3\sigma$. These spectra are analyzed further by Riechers et al. 2013 (in preparation).

Two of our targets, LSW 48 and LSW 52, were observed with Bolocam at 1.1 mm in December 2012 under excellent conditions ($\tau_{225GHz}$(zenith) = 0.03 – 0.06) using a Lissajous scan pattern. Bolocam is a facility 144-element bolometer camera at the CSO that can operate at either 1.1 or 2.1 mm (Glenn et al. 2003). The beam FWHM at 1.1 mm is 31″, and the fractional bandwidth is 0.17. The total integration time for LSW 48 was 2.0 hrs, and for LSW 52 was 4.3 hrs. The reduction procedures are as described in Wu et al. (2012). Both sources
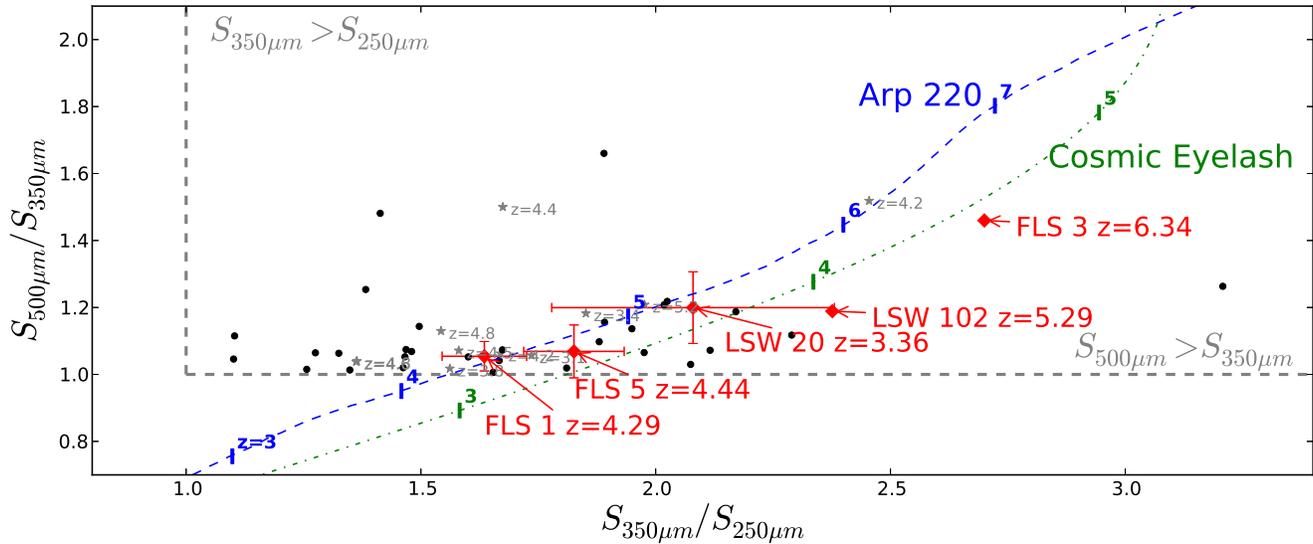
**Figure 5.** SPIRE color ratios for sources presented in this paper (black dots). The sources with redshifts are shown as red diamonds. For comparison, $500\,\mu m$-riser sources with redshifts selected via other methods (i.e., not on the basis of their SPIRE colors) are shown as gray stars (see §6). SED tracks based on Arp 220 and the Cosmic Eyelash (Swinbank et al. 2010) are shown for comparison. They gray dashed lines represent our selection in color space. Note that the uncertainties vary considerably, and are quite large for some of the sources. Example uncertainties are shown for FLS 1, 5, and LSW 20.
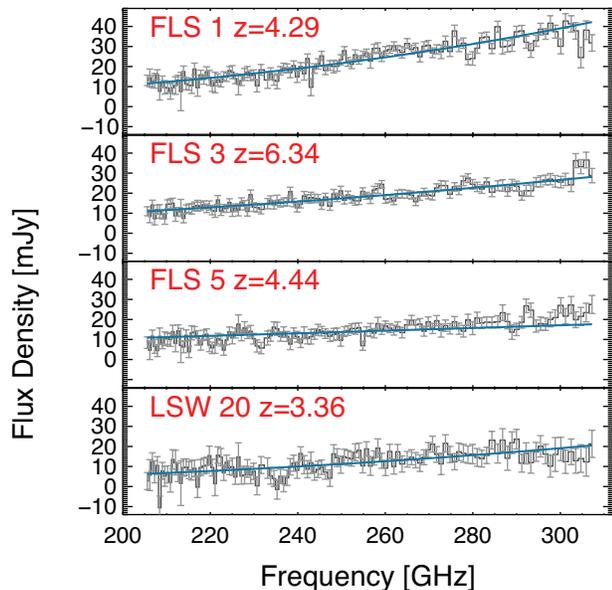


**Figure 6.** Z-Spec observations of our sources. All four have known redshifts from either CARMA or Keck as described in the text. Line searches in these data will be discussed in Riechers et al. 2013, in preparation.

were detected, and are unresolved by the Bolocam beam.

### 4.3. *Sub-mm/mm Interferometric Continuum Observations: SMA and PdBI*

Four sources (FLS 1, FLS 3, FLS 5, and LSW 20) were observed with the Submillimeter Array (SMA) at $\lambda = 1.1$ mm using a combination of compact, sub-compact, and extended configurations. Similarly, nine of our targets (FLS 1, FLS 3, FLS 6, FLS 17, FLS 19, LSW 20, LSW 28, LSW 29, and LSW 102) were observed with the Plateau de Bure Interferometer (PdBI) at $\sim 1.3$ mm. In the majority of the cases – including all five with redshifts – the large millimeter-wave fluxes are confirmed,

and in most cases the emission at $3''$ resolution is dominated by a single spatial component. Further details of these observations, including source morphologies and more precise interferometric positions, will be presented by Clements et al. (in preparation) and Perez-Fournon et al. (in preparation), respectively.

The SMA and PdBI detections allow us to measure the positional accuracy of our SPIRE detections. For those sources – which tend to be the brighter members in the sample – the median separation of the interferometric source and the centroid of the source in the SPIRE difference map is $5.1''$. For sources which are isolated and clearly detected in the 250 or $350\,\mu m$ bands, a significantly better SPIRE position can be derived by using those images alone. For fainter and blended sources, the positional accuracy is probably somewhat worse.

The SMA and PdBI flux densities of 8 of our sources were measured from Gaussian fits in the *uv*-plane, and are given in Table 4; final flux densities for the other sources are awaiting the completion of all scheduled observations. LSW 20 is resolved into two sources with a separation of $\sim 3.8''$ by the SMA observations (also see §4.5). Because the SPIRE and Z-Spec beams are much larger than this ($> 18''$), we add the flux densities of the two components for our analysis. The PdBI observations of this source also show indications of a faint component at the same position, but the flux density is poorly constrained. Combined with the Z-Spec and Bolocam observations, we can see that, with the exception of FLS 17, our targets are among the strongest known optically-faint dusty galaxies at $\lambda \approx 1$ mm that are not known to be significantly lensed.

### 4.4. *Radio Continuum Observations*

FLS 3 was the subject of deep targeted Jansky Very Large Array (JVLA) and follow-up at 21cm once its redshift was determined (Riechers et al. 2013). A radio source is detected at $6\sigma$ in the deep Morrison et al.

(2010) JVLA survey of GOODS-N close to the position of GOODSN 8. There are no other detected sources within $15''$. However, without a precise sub-mm/mm interferometric position for this source (unlike FLS 3), we are unable to determine if this is, in fact, a radio detection of our source. LSW 26, which lies within the region covered by the deep Owen & Morrison (2008) 20 cm survey of the Lockman-Hole, is not detected in those data, but without knowing the source size the exact detection limit is uncertain.

Enhanced Multi-Element Radio Linked Interferometer Network (e-MERLIN) observations of four of the sources in this paper (FLS 1, FLS 3, FLS 5, and LSW 20) were carried out in March 2012. A central tuning of 1.55 GHz with an instantaneous bandwidth of 348 MHz was used. All seven stations were available, resulting in a $0.3''$ synthesized beam. 3C286 was used as the primary flux calibrator and OQ208 was used as the bandpass calibrator. The sources were observed for 6 hours each from 26th - 30th of March 2011. The data were flagged spectrally, averaged in frequency, fringe fitted and then calibrated using standard methods for phase referencing experiments. However, none of the sources were detected, with map RMS value of $15 - 18 \mu$Jy.

We can compare these observations with those predicted by the far-IR/radio correlation, which is parameterized by $q_{IR}$, the logarithmic ratio of $L_{IR}$ and the 1.4 GHz flux density. The lack of redshifts, as well as the poor constraints on $L_{IR}$ in the absence of Rayleigh-Jeans-side (longer-$\lambda$) data (Table 3), make this comparison uninformative for GOODSN 8 and LSW 26. For the other sources, if we assume $S_\nu \propto \nu^{-0.8}$ in the radio, and adopt the value for $q_{IR}$ measured for $z \sim 2$ *Herschel*-selected DSFGs from Ivison et al. (2010), we can predict the range of expected $S_{1.55\,GHz}$ flux densities for comparison with our detection limits. Including the scatter in $q_{IR}$ and the measurement uncertainties in each $L_{IR}$, we predict 95% central confidence limits of 50-324, 15-94, 21-151, and $15 - 116 \mu$Jy for FLS 1, FLS 3, FLS 5, and LSW 20, respectively. The non-detections of FLS 3, FLS 5 and LSW 20 are consistent with the far-IR/radio correlation, while FLS 1 is fainter in the radio than expected at moderate significance. However, the e-MERLIN non-detection of FLS 3 also disagrees with the JVLA 1.4 GHz measurement ($S_{1.4\,GHz} = (59 \pm 11)\mu$Jy), which is consistent with the far-IR/radio correlation (Riechers et al. 2013). This discrepancy suggests that e-MERLIN may be partially resolving out the radio emission for these sources.

### 4.5. *Optical Spectroscopy: Keck and GTC*

In addition to the sub-mm through radio observations, FLS 1 and LSW 20 were targeted for optical spectroscopy in July 2010 and May 2011 using the Low Resolution Imaging Spectrograph (LRIS; Oke et al. 1995) on the Keck I 10 m telescope, making use of their high-precision SMA interferometric positions. We utilized a $1''$ slit width, and the D560 dichroic with the 4000Å, 600 line mm$^{-1}$ grism (blue side) and 400 line mm$^{-1}$ grating (red side) blazed at $\sim$7800Å. The data were binned ($1 \times 2$) in the spectral direction on the blue side and unbinned on the red, providing similar wavelength dispersions of 1.26 and 1.16Å per pixel, respectively. The

targets were observed with median seeing of $\sim 1\rlap{.}''0$, with a total integration time of 2.2 and 1.2 hrs, respectively. The LRIS data were reduced using standard `IRAF` procedures. No continuum or emission lines were detected toward the SMA position for FLS 1. However, spectroscopy of LSW 20 (Figure 7) reveals multiple emission lines from both a foreground $z = 0.352$ and high redshift $z = 3.358$ galaxy, both toward the brighter component in the SMA image. No continuum or emission lines were detected from the fainter SMA component. This possible lensing system will be discussed further elsewhere. FLS 3 was also observed with LRIS, as discussed in Riechers et al. (2013).

Optical spectroscopic observations of FLS 1 were also carried out on 16 May 2013 (UT) using the Optical System for Imaging and low Resolution Integrated Spectroscopy (OSIRIS)[43] on the Gran Telescopio Canarias (GTC) 10.4m telescope. Observing conditions were photometric, with a median seeing of $0.75''$, and the total integration time was 1.5 hrs. We utilized a $1.2''$ slit width, and the high throughput R2500R VPH grism, which provides a spectral range of 5630 - 7540 Å and a wavelength dispersion of 1.04 Å per pixel. The slit was positioned at an angle of 343.5 deg including a faint optical object close to the radio interferometric position and a faint galaxy at 1 arcmin to the NW. No continuum or emission lines were detected close to the FLS 1 position. However, faint continuum and emission lines were detected at RA 17h08m15.727s, Dec +58d29m29.35s, about $52''$ from FLS 1 and $8''$ from the galaxy used to position the slit. Careful analysis of the 2D spectrum at this position reveals emission lines (H$\beta$ and [O III] 4959, 5007 Å ) from a low redshift galaxy at $z = 0.415$ and a narrow line at 6430 Å which we identify as Lyman$\alpha$ at $z = 4.287$ (Figure 8), very close to the CO redshift of FLS 1 ($z = 4.286$; see below). The serendipitous detection of a galaxy at the same redshift as FLS 1 in a narrow long-slit is highly improbable unless there is an overdensity of galaxies close to FLS 1 as detected around other high redshift SMGs (e.g. Capak et al. 2011). The GTC observations will be presented in more detail elsewhere.

### 4.6. *CARMA Millimeter-Wavelength Line Search*

Five of our sources have been observed with CARMA with the main goal of redshift detection. These observations are described by Riechers et al. 2013 (in preparation). The redshift for LSW 20 has been confirmed with a CO line; the measured CO value is $z = 3.32$, corresponding to a relative velocity of 2600 km/s in the source frame with respect to the optical redshift. The source of this discrepancy is currently not clear. FLS 1 has a redshift of 4.29 based on two CO lines. FLS 3 has a redshift of 6.34 based on multiple emission lines (Riechers et al. 2013). FLS 5 has a redshift of 4.44 based on multiple CO lines, and LSW 102 has a redshift of 5.29 based on clear detections of CO J(6-5), (5-4), and [N II] 205 $\mu$m. The uncertainties in these redshifts are negligible for the purposes of this paper.

### 4.7. *Fits to SPIRE plus Sub-mm/mm Photometry*

---

[43] http://www.gtc.iac.es/instruments/osiris/osiris.php
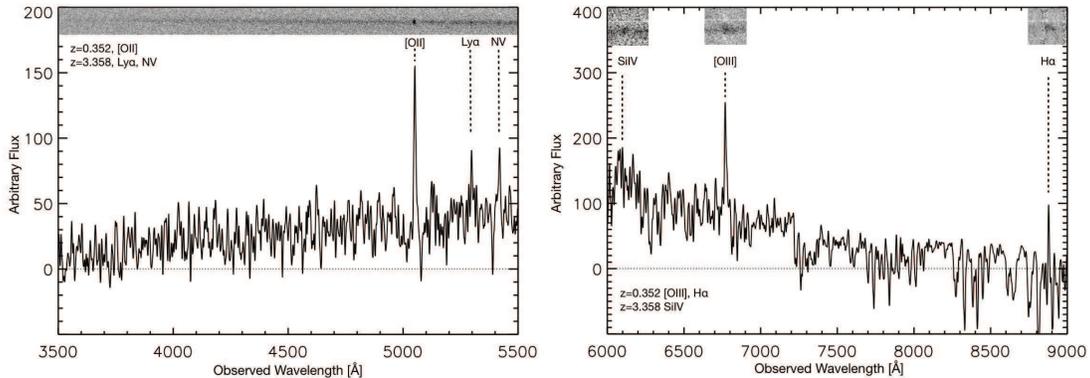
**Figure 7.** The blue (left) and red (right) Keck/LRIS spectra of LSW 20. Two sources are detected in multiple lines – a $z = 0.352$ foreground source, and a background $z = 3.358$ source. The CO redshift of the DSFG is $z = 3.32$.

**Table 4**
Additional follow-up

| Source | Optical | Z-Spec | | | | | Bolocam | SMA | PdBI | Radio |
| | | $S_{1016\,\mu m}$ | $S_{1113\,\mu m}$ | $S_{1210\,\mu m}$ | $S_{1311\,\mu m}$ | $S_{1411\,\mu m}$ | $S_{1.1\,mm}$ | $S_{1.1\,mm}$ | $S_{1.3\,mm}$ | |
|---|---|---|---|---|---|---|---|---|---|---|
| FLS 1 | ✓ | $34.1 \pm 0.7$ | $28.3 \pm 0.7$ | $21.8 \pm 0.5$ | $15.0 \pm 0.6$ | $12.1 \pm 0.8$ | $\cdots$ | $13.8 \pm 0.8$ | $14.5 \pm 0.9$ | ✓ |
| FLS 5 | | $20.3 \pm 0.7$ | $16.6 \pm 0.5$ | $12.5 \pm 0.6$ | $11.4 \pm 0.6$ | $9.5 \pm 0.7$ | $\cdots$ | $17.2 \pm 1.1$ | $\cdots$ | ✓ |
| LSW 20 | ✓ | $16.8 \pm 1.1$ | $14.9 \pm 0.8$ | $12.0 \pm 0.8$ | $7.0 \pm 0.9$ | $7.2 \pm 1.1$ | $\cdots$ | $18.4 \pm 1.3$ | $8.7 \pm 1.8$ | ✓ |
| FLS 6 | | $\cdots$ | $\cdots$ | $\cdots$ | $\cdots$ | $\cdots$ | $\cdots$ | $\cdots$ | $8.4 \pm 0.6$ | |
| FLS 17 | | $\cdots$ | $\cdots$ | $\cdots$ | $\cdots$ | $\cdots$ | $\cdots$ | $\cdots$ | $1.5 \pm 0.4$ | |
| FLS 19 | | $\cdots$ | $\cdots$ | $\cdots$ | $\cdots$ | $\cdots$ | $\cdots$ | $\cdots$ | $9.1 \pm 0.8$ | |
| LSW 29 | | $\cdots$ | $\cdots$ | $\cdots$ | $\cdots$ | $\cdots$ | $\cdots$ | $\cdots$ | $8.4 \pm 1.9$ | |
| LSW 48 | | $\cdots$ | $\cdots$ | $\cdots$ | $\cdots$ | $\cdots$ | $13.0 \pm 2.4$ | $\cdots$ | $\cdots$ | |
| LSW 52 | | $\cdots$ | $\cdots$ | $\cdots$ | $\cdots$ | $\cdots$ | $7.5 \pm 1.6$ | $\cdots$ | $\cdots$ | |

Note. — Additional observations for our sources. The optical spectroscopy and radio observations are discussed in §4.5 and §4.4, respectively. The mm-band flux densities are given in mJy, and only instrumental noise is included in the quoted uncertainties. Observations of FLS 3 are described in Riechers et al. (2013). Sources in the top portion of the table have known redshifts. The SMA flux density for LSW 20 is the sum of the two components, but for PdBI is only for the brighter of the two components. The Z-Spec flux densities are binned into five equal sized bins in wavelength.
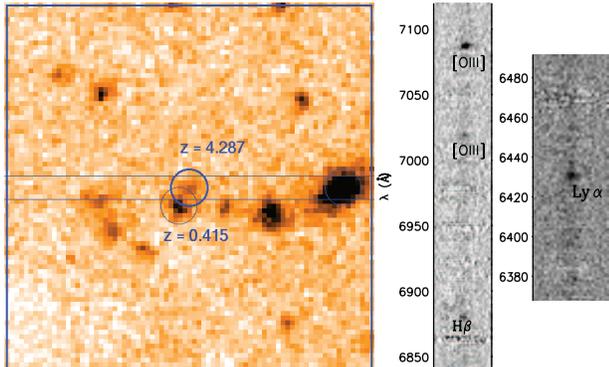


**Figure 8.** GTC observations of galaxies near FLS 1. The left panel shows a GTC $z$-band image of the field around a high redshift galaxy discovered during the long-slit observations of FLS 1. The spectra of two galaxies overlap in the long-slit spectrum. The slit is shown by the horizontal lines, and the circled galaxy on the right was used to align the slit. The middle panel shows the 2D GTC OSIRIS spectrum of the $z = 0.415$ galaxy showing emission lines of H$\beta$ and [O III] 4959, 5007 Å, and the right panel the spectrum of the $z = 4.287$ galaxy showing narrow Ly$\alpha$ emission. FLS 1 is $30''$ outside the frame of the $z$-band image.

Here we present modified blackbody fits to FLS 1, FLS 5, and LSW 20, all of which have known redshifts and mm-band observations to constrain the red side of the thermal SED. We use the same MCMC code as described in §3 and the Appendix, but omit the priors on $\beta$ and $\lambda_0$. A similar analysis for FLS 3 is presented by Riechers et al. (2013). The mm-band observations of

LSW 102 are ongoing. We use the results to constrain the dust temperature, far-IR luminosity (and hence star-formation rate), and dust mass for these sources. The calibration uncertainties and confusion noise are handled as previously for SPIRE data. In addition, we assume 10% calibration uncertainties for SMA, PdBI, and Z-Spec that are uncorrelated between observatories, but are perfectly correlated between the Z-Spec channels. Given the high resolution of the interferometric observations, we do not include confusion noise for the SMA or PdBI observations, since it is negligible compared with the other uncertainties. We expand our estimates of the correlation in the confusion noise to the binned Z-Spec channels using the same simulations as for the SPIRE bands. The Z-Spec and SMA 1.1 mm flux densities for FLS 1 disagree significantly. We have been unable to determine why this is the case, but given the good agreement for this source between the Z-Spec and PdBI 1.3 mm observations, we do not use the SMA observations for this source. As noted in §3, the blue-side power law ($\lambda^\alpha$), does not improve our fits.

In addition to the SED parameters, we measure $L_{IR}$ (the integrated IR luminosity between 8 and $1000\,\mu m$ in the rest frame), and the dust mass, $M_d$. For these calculations, and elsewhere in this paper, we assume a flat Universe and a cosmological constant with $\Omega_m = 0.27$ and $H_0 = 70\,\mathrm{km\,s^{-1}\,Mpc^{-1}}$. The dust mass is estimated

using

$$M_{\rm d} = S_\nu D_{\rm L}^2 \left[(1+z)\,\kappa_\nu B_\nu\right]^{-1} \tau_\nu \left[1 - \exp\left(-\tau_\nu\right)\right]^{-1},$$

where $S_\nu$ is the flux density, $D_{\rm L}$ the luminosity distance, $\kappa_\nu$ the mass absorption coefficient, $\tau_\nu$ the optical depth, and $B_\nu$ the Planck function, with all quantities expressed in the observer frame. For the mass absorption coefficient we adopt $\kappa_\nu = 2.64\,{\rm m}^2\,{\rm kg}^{-1}$ at $125\,\mu{\rm m}$ (rest frame, Dunne, Eales, & Edmunds 2003). Our quoted uncertainties on $M_{\rm d}$ do not include the uncertainty in $\kappa_\nu$, which is at least a factor of 0.3 dex. To compute the star formation rate, we use the relation of Kennicutt (1998), which assumes a Salpeter IMF. Note that $L_{\rm IR}$, $M_{\rm d}$, and the star formation rate assume no lensing magnification. Lensing constraints from interferometric observations will be described in future papers.

The results of these fits are given in Table 5 and shown in Figure 9. The derived properties of these sources ($T_d$, $\beta$) are fairly typical of the most luminous *Herschel*-selected DSFGs at lower $z$. The $\beta$ values are somewhat higher than usual, but consistent, given the uncertainties, with the often assumed value $\beta = 2$. Due to the large uncertainties in $\beta$ for LSW 20, $M_{\rm d}$ and the area of emission ($A_{\rm em}$) are not well constrained, so only lower limits on these two quantities are provided. The $\chi^2$ values are acceptable for all fits. The fits favor using an optically thick model, with a typical decrease in the $\chi^2$ of about 3 for adding one additional parameter. However, the data are not sufficient to rule out an optically thin model for any of these sources.

The derived $L_{\rm IR}$ values suggest that these sources are among the most luminous IR sources known (assuming no magnification). Unlike FLS 3 (Riechers et al. 2013), where the data is consistent with an optically thin model, the SEDs for all three sources presented here moderately favor becoming optically thick near $200\,\mu{\rm m}$ (rest-frame). Therefore, CO excitation modeling of these sources may have to consider extinction.

## 5. THE NUMBER DENSITY OF RED SPIRE SOURCES

In order to estimate the space density of bright, red SPIRE sources, we must determine both how efficient our selection is at finding red sources and the expected false detection rate. Given the modest number of sources detected, and the large observational uncertainties in the SPIRE colors, we do not attempt to measure the differential number counts as a function of color or flux density, but simply the number of sources per ${\rm deg}^2$. If we denote the efficiency for the detection of the $i^{\rm th}$ source by $\epsilon_i$ and the expected purity of our catalog by $p$ (so $1 - p$ is the fraction of the detected sources that do not belong in our sample), then the space density of sources $N$ is

$$N = \frac{p}{A} \sum_i \frac{1}{\epsilon_i}, \qquad (4)$$

where $A$ is the area of the survey and the sum is over the sources in our final catalog. We now discuss how we compute $\epsilon_i$ and $p$.

### 5.1. *Efficiency*

Our approach for computing the efficiencies is to work as closely as possible with the observables rather than

try to compress the information by assuming some SED model and reducing the problem to a smaller number of variables (e.g., assuming an optically thin, fixed $\beta$ modified blackbody and computing $\epsilon$ as a function of $T_d$ and a suitable normalization variable). It is not clear how well the data are described by such simple models, particularly on the blue side of the thermal SED (see, e.g., Blain, Barnard, & Chapman 2003). Furthermore, even if they were perfectly described in the mean by such a simple model, the degree of intrinsic deviation of individual DSFGs from such models is not well characterized.

Therefore, we measure the efficiency directly using the observed flux density of each source in the SPIRE bands, which should be significantly more accurate than using an SED model. Because our efficiency is a complicated mix of these variables, however, we can not make any statement that we are complete up to some simply expressible threshold. Thus, while our model should be substantially better than one based on a simple SED model, it is not trivial to visualize how $\epsilon$ depends on the SPIRE flux densities.

Therefore, purely for this purpose, we illustrate our selection efficiency for a modified blackbody SED model as a function of temperature and $S_{500\mu{\rm m}}$ in Figure 10, using the approach detailed below. The model is an optically thin modified blackbody coupled with a $nu^{-\alpha}$ power law (on the Wien side, fixing $\beta = 1.5$ and $\alpha = 4$ based on the properties of nearby (hence well observed) IR-luminous galaxies. Note that many of our actual sources are not well fit by these parameters, and so we do not use this model in any way while computing the actual detection efficiencies. This figure does, however, correctly illustrate that the detection efficiency decreases quite rapidly at low flux densities, which is the basis of our selection requirement $S_{500\mu{\rm m}} \geq 30$ mJy.

Due to the relatively small number of sources in our catalog, rather than attempt to compute the efficiencies on a grid of the three flux densities (for each field) and then interpolate, it is more efficient to compute them individually for each source. Our basic tool for doing so is, for each source in our catalog, to inject false sources into the actual maps for each field with properties that match the measurements of each source, and then determine how many are recovered using the search pipeline.

An important point is that we do not know the precise flux densities of any source due to observational uncertainties (instrument and confusion noise), and therefore each efficiency has an associated uncertainty which can not be reduced without additional observations. We include this effect in our simulations by generating a moderate number ($N_\sigma$) of flux density triplets for each source drawn from a multi-variate Gaussian centered on the observed flux densities and using the estimated uncertainties. We then carry out $N_{\rm sim}$ simulations for each of the flux density triplets, each of which has $N_{\rm src}$ sources injected, averaging to form $N_\sigma$ estimates of $\epsilon$ for each source. The final $\epsilon$ is then the average of the $N_\sigma$ values, and the uncertainty is given by the distribution of values.

$N_\sigma$ does not have to be very large to provide a good estimate of the uncertainty, and so we generally adopt a value of $N_\sigma = 60$, except for a few sources where we used $N_\sigma > 1500$ in order to verify convergence. $N_{\rm src}$ is limited by the desire to avoid two sources overlapping within the matching radius, $m_{\rm rad}$. We have conservatively adopted

**Table 5**
Fits to sources with known redshifts.

| Parameter | Value | Description | Note |
|---|---|---|---|
| | | FLS 1, $z = 4.29$ | |
| $\chi^2$ | 4.83 | $\chi^2$ | 5 DOF; $P\left(>\chi^2\right) = 0.44$ |
| $T_{\rm d}$ | $63^{+3}_{-4}$ K | Dust temperature | |
| $\beta$ | $2.8 \pm 0.6$ | Extinction slope | |
| $f_{500\,\mu\rm m}$ | $91 \pm 11$ mJy | Normalization at $500\,\mu$m | Observer frame |
| $\lambda_0$ | $200^{+26}_{-23}\,\mu$m | $\lambda$ where $\tau = 1$ | Rest frame |
| $\alpha$ | $> 3.6$ | Blue side power-law slope | 68.3% limit |
| $L_{\rm IR}$ | $5.6^{+0.7}_{-0.9} \times 10^{13}$ L$_\odot$ | IR luminosity | 8–1000 $\mu$m (rest frame) |
| $M_{\rm d}$ | $5.1^{+1.6}_{-2.4} \times 10^9$ M$_\odot$ | Dust mass | |
| SFR | $9700^{+1200}_{-1600}$ M$_\odot$ yr$^{-1}$ | Star formation rate | |
| $A_{\rm em}$ | $82^{+12}_{-21}$ kpc$^2$ | Dust emission area | |
| | | FLS 5, $z = 4.44$ | |
| $\chi^2$ | 2.5 | $\chi^2$ | 4 DOF; $P\left(>\chi^2\right) = 0.64$ |
| $T_{\rm d}$ | $59 \pm 6$ K | Dust temperature | |
| $\beta$ | $1.7 \pm 0.5$ | Extinction slope | |
| $f_{500\,\mu\rm m}$ | $47 \pm 7$ mJy | Normalization at $500\,\mu$m | Observer frame |
| $\lambda_0$ | $191 \pm 62\,\mu$m | $\lambda$ where $\tau = 1$ | Rest frame |
| $\alpha$ | $> 3.9$ | Blue side power-law slope | 68.3% limit |
| $L_{\rm IR}$ | $2.8^{+0.5}_{-0.6} \times 10^{13}$ L$_\odot$ | IR luminosity | 8–1000 $\mu$m (rest frame) |
| $M_{\rm d}$ | $2.0^{+0.6}_{-0.8} \times 10^9$ M$_\odot$ | Dust mass | |
| SFR | $4800 \pm 900$ M$_\odot$ yr$^{-1}$ | Star formation rate | |
| $A_{\rm em}$ | $67^{+26}_{-31}$ kpc$^2$ | Dust emission area | |
| | | LSW 20, $z = 3.36$ | |
| $\chi^2$ | 6.0 | $\chi^2$ | 5 DOF; $P\left(>\chi^2\right) = 0.31$ |
| $T_{\rm d}$ | $48 \pm 6$ K | Dust temperature | |
| $\beta$ | $2.8 \pm 1.2$ | Extinction slope | |
| $f_{500\,\mu\rm m}$ | $41 \pm 8$ mJy | Normalization at $500\,\mu$m | Observer frame |
| $\lambda_0$ | $210 \pm 59\,\mu$m | $\lambda$ where $\tau = 1$ | Rest frame |
| $\alpha$ | $> 3.9$ | Blue side power-law slope | 68.3% limit |
| $L_{\rm IR}$ | $1.1^{+0.2}_{-0.3} \times 10^{13}$ L$_\odot$ | IR luminosity | 8–1000 $\mu$m (rest frame) |
| $M_{\rm d}$ | $> 2.0 \times 10^9$ (95%) | Dust mass | |
| SFR | $1900^{+300}_{-500}$ M$_\odot$ yr$^{-1}$ | Star formation rate | |
| $A_{\rm em}$ | $> 32$ kpc$^2$ (95%) | Dust emission area | |

**Note**. — The results of modified blackbody fits to FLS 1, FLS 5, and LSW 20, as detailed in the text. $L_{\rm IR}$, $M_{\rm d}$, $A_{\rm em}$, and the SFR assume no lensing magnification.
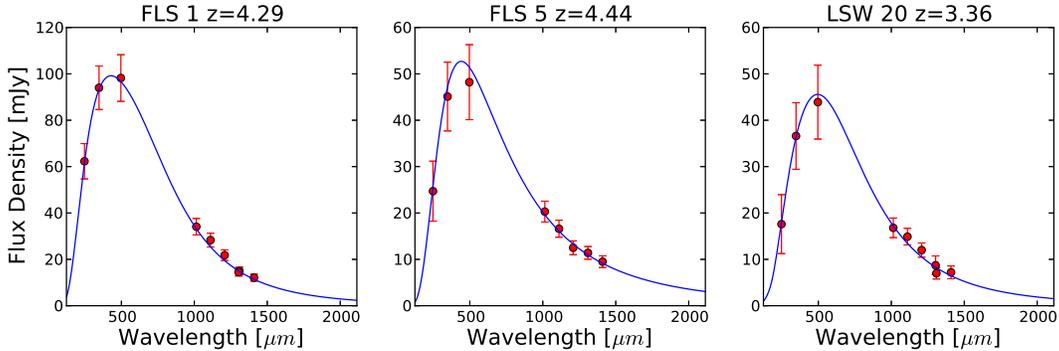


**Figure 9.** Modified blackbody dust SED fits to sources with known redshifts, as described in §4.7. The displayed uncertainties include calibration and confusion noise.

$m_{\rm rad} = 15''$, compared with the typical positional uncertainty of $5''$ for our faintest sources in simulations (and from interferometric observations: §4.3). With these values, the correction for sources lost due to positional uncertainties are negligible compared with our other uncertainties. We adopt $N_{\rm src} = 800$ for our FLS simulations, $N_{\rm src} = 2500$ for those of the combined Lockman fields, and $N_{\rm src} = 50$ for GOODS-N, which limits the effects of overlap on the recovered counts to less than 1%, again much smaller than our other sources of uncertainty. It is

important that $N_{\rm sim} \times N_{\rm src}$ is large enough that $\epsilon$ is measured for each flux triplet to much better precision than the variation between flux triplets for the same source. We have adopted $N_{\rm sim} = 60, 30, 800$ for FLS, Lockman, and GOODS-N, respectively, based on tests with much larger $N_{\rm sim}$ values. In total, therefore, the efficiency for each FLS source is based on 2.4 million injected sources, GOODS-N on 2.4 million, while in Lockman that value is 4.5 million; more sources are desirable for the Lockman fields because the noise properties of the map are
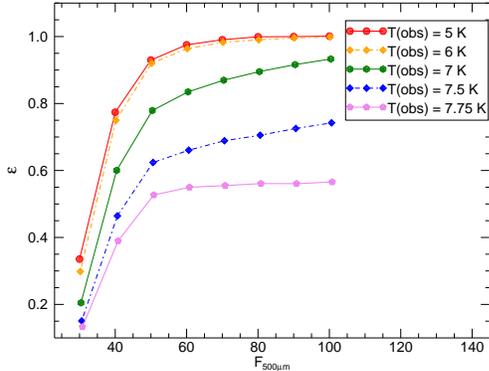
**Figure 10.** Illustration of our selection efficiency for a simple optically thin modified blackbody (with $\beta = 1.5$) plus blue-side power law model ($S_\nu \propto \nu^{-4}$) as a function of $S_{500\mu m}$ and the observer frame dust temperature $T(\mathrm{obs}) = T_d/(1+z)$. The color ratios are a strong function of temperature, and, for these values of $\beta$ and $\alpha$, sources with $T(\mathrm{obs}) > 7.75$ K are not "red". For sources with $S_{350\mu m} \simeq S_{500\mu m}$ the selection efficiency is relatively independent of flux density, since the dominant factor is the uncertainty in whether the source actually satisfies $S_{500\mu m} \geq S_{350\mu m}$ due to instrument and confusion noise. These simulations were carried out for the FLS field.
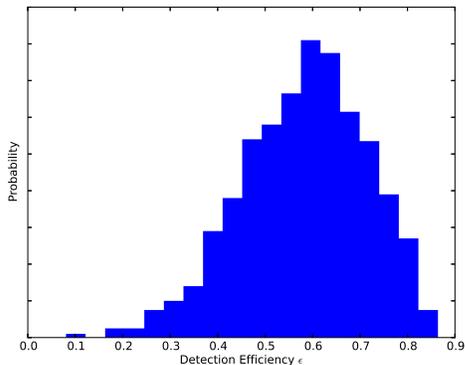


**Figure 11.** Histogram of efficiencies ($\epsilon$) for FLS 5. Each entry represents a different flux density triplet reflecting the observational (instrumental and confusion) uncertainties. For this source, $N_\sigma = 1500$ simulations were carried out. The resulting efficiency has significant non-Gaussian tails.

less uniform.

The resulting efficiencies and uncertainties are provided in Table 3. They range from $\sim 90\%$ for FLS 3 (the $z = 6.34$ source) to $\sim 20\%$ for faint sources with $S_{500\mu m} \simeq S_{350\mu m} \simeq S_{250\mu m}$. The uncertainties in each $\epsilon_i$ are generally non-Gaussian (Figure 11), especially for sources with $S_{500\mu m} \simeq S_{350\mu m}$. We use the measured $\epsilon$ distribution for each source when computing the source density, as discussed below. Again, note that the uncertainties in the $\epsilon$s primarily arise from the uncertainties in the flux densities of each source, not from the finite number of simulations we carried out, and hence are irreducible given current observations.

## 5.2. *Purity*

There are two classes of contaminants in our analysis: faint red sources below our $S_{500\mu m} \geq 30$ mJy cut, and non-red sources. The effects of the former are com-

monly referred to as 'boosting' or 'Eddington bias' in the sub-mm/mm literature, and can be caused by both instrument noise and blending effects, while those of the latter almost entirely arise from instrument noise because blending tends to make sources bluer. The rate of contamination of fainter sources is easy to estimate using the same methods as in §5.1, but the second is much more difficult to characterize. False detections caused by map artifacts, evaluated through jack-knife tests on our maps, are negligible.

### 5.2.1. *Boosting*

There are two ingredients required to estimate the contamination by red but faint ($S_{500\mu m} < 30$ mJy) sources: a measurement of the efficiency of detecting such sources; and an estimate of their number density. For the former, we use the same technique as in the previous section to measure the detection efficiency as a function of $S_{500\mu m}$, omitting the $N_\sigma$ sampling over photometric errors. Here we must assume SPIRE color ratios. We adopt the median of our catalog sources, $S_{500\mu m}/S_{350\mu m} = 1.09$ and $S_{500\mu m}/S_{250\mu m} = 1.88$, and later check to see how changing these values affects our results. The detection efficiency would be essentially zero in the absence of boosting effects, and is a strong function of $S_{500\mu m}$. We perform a series of simulations, sampling $S_{500\mu m}$ from 29 to 2 mJy in 1 mJy steps. As expected, the recovery efficiency falls quite rapidly, from 8.9% at $S_{500\mu m} = 29$ mJy to $< 0.01\%$ at 5 mJy, crossing 1% at 18 mJy. We carry out separate simulations for each field with at least 250,000 sources per mJy bin per field, and find that the values are essentially identical for all fields.

Unfortunately, we do not yet have good measurements of the number counts of red sources, especially at faint flux densities. Our approach is therefore to scale from the observed SPIRE number counts, which are expected to be dominated by sources at lower $z$. Assuming our source population has $\langle z \rangle = 4.7$ (§7.4), a flux cut of $S_{500\mu m} \geq 30$ mJy corresponds to a cut of $S_{350\mu m} \geq 61$ mJy at $z = 3$, or $S_{250\mu m} \geq 140$ mJy at $z = 1.9$. The DSFG population is thought to peak closer to $z = 3$ (Chapman et al. 2005; Weiß et al. 2013), so we adopt the $350\,\mu m$ counts for our calculations, using the $250\,\mu m$ value as a comparison to estimate the uncertainty. For these calculations we adopt the differential number counts in each band from Oliver et al. (2010), normalizing them to match the observed number of red sources.

Using the above ingredients, we find an expected boosting contamination of 0.8 sources in FLS, 1.4 in Lockman-SWIRE, and $\ll 1$ in GOODS-N, Lockman-East, and Lockman-North. In all cases these correspond to $\sim 0.1$ deg$^{-2}$, a small value compared to the catalog source density of $> 2$ deg$^{-2}$. Making the simulated sources as red as FLS 3 (our $z = 6.3$ source, and one of the reddest sources in the sample) increases this value by only 0.03 deg$^{-2}$. Using the $250\,\mu m$ counts decreases it by 0.02 deg$^{-2}$, and using the shape of the number counts from the B11 model at $z > 3$ increases it by 0.05 deg$^{-2}$. We therefore adopt a value for the contamination by faint red sources below our flux density cutoff of $0.11 \pm 0.06$ deg$^{-2}$, which is negligible compared with the other sources of uncertainty.

### 5.2.2. *Non-red Contaminants*

The basic tool for our analysis of contamination by non-red sources is again simulations, but here rather than injecting sources into real maps we generate simulated maps based on models of the DSFG population, but with intrinsically red, bright sources omitted, and run our search pipeline on those maps. The most common type of false detections, according to models, are *nearly*-red ("orange") sources combined with noise fluctuations or blended with faint red sources. Therefore, the critical model ingredient is the number of almost-red sources. Unfortunately, it is not clear how well current models represent this population, given that, as discussed later, they generally significantly under-predict the number of truly red sources.

There are a number of such models in the literature. However, as shown by Oliver et al. (2010); Glenn et al. (2010); Clements et al. (2010), pre-*Herschel* models do a poor job of reproducing the observed number counts at $250$–$500\,\mu$m, and therefore are not a good choice for our simulations. We instead make use of the post-*Herschel* backward-evolution B11 model, which is a good match to current number count constraints. For each field, we generate a number of simulations using this model with genuinely red sources brighter than $S_{500\mu\mathrm{m}} = 3$ mJy removed, adding the measured noise at each position of the map. Simply distributing the sources randomly (i.e., in an unclustered fashion) will underestimate the false detection rate, so we include clustering using the measured $350\,\mu$m power spectrum of Amblard et al. (2011); note that this is purely clustering in the plane of the sky. If "orange" sources are more strongly clustered on the sky, then this may underestimate contamination effects. However, increasing the simulated clustering by a factor of three does not have any measurable effect on our false detection results. We generate 200 simulations of each field, and then run them through the same detection pipeline as the real data, and then count the number of sources detected.

We visually inspect all of our actual catalog sources to note blends. We therefore must carry out the same procedure on at least a subset of our purity simulations. Doing so for 100 simulated maps of each field removes approximately half the detected sources – more precisely 83 out of 145 in FLS, and 174 of 320 in Lockman-SWIRE. These are all blends of sources which can clearly be identified in the un-smoothed maps, and where the individual constituents are too faint to belong in our catalog. This blend rate – 2.6 sources for FLS and Lockman-SWIRE combined – is consistent with the observed number (two) in our catalog. The false detection rates for the smaller, deeper fields (Lockman-North, Lockman-East, and GOODS-N) are less than 0.3 per field.

The purity is then given by $p = (N_{\mathrm{cat}} - N_{\mathrm{false}})/N_{\mathrm{cat}}$, where $N_{\mathrm{cat}}$ is the number of sources in our catalog for a given field, and $N_{\mathrm{false}}$ is the estimated number of false detections from simulations of the same field. Note that $N_{\mathrm{false}}$ is determined much more precisely than $N_{\mathrm{cat}}$, which suffers from Poisson noise. We conclude that the purity of our catalog sample is approximately 90%, somewhat higher in FLS (93%) and somewhat lower in Lockman-SWIRE (91%). Interestingly, increasing the S/N requirement for detection to 5, 6, or 7 does not have much effect on the purity – while increasing the S/N requirement cuts down the number of false sources

in simulations, it removes a large a fraction of real sources from the actual maps. Some of the false detections, due to unresolved blends, are as bright as 80 mJy at $500\,\mu$m. Decreasing the S/N requirement to 3, on the other hand, decreases the purity to 75%, so our value of 4 is a good compromise. Note that this appears to be true for all our fields, despite their range of depths.

During the preparation of this paper but too late to be used as the primary model for our purity simulations, the B11 model was updated (Béthermin et al. 2012, hereafter B12). The B12 model predicts significantly more "orange" sources than the B11 model, implying a lower purity fraction for our catalog. Based on $40\,\mathrm{deg}^2$ of simulated data (compared with the several hundred for the B11 model), we find a predicted number density of "orange" interlopers of $0.41\,\mathrm{deg}^{-2}$, corresponding to a purity of $\sim 80\%$. In the future, once more models have been updated to reflect the *Herschel* number counts, it will be helpful to compare the false detection rates for different models to estimate the systematic uncertainties in the purity. The parameters of the B11 model do have estimated uncertainties, but adjusting the model parameters to increase the number of red (and near-red) sources by those uncertainties does not produce any detectable change in the purity rate. It seems likely that the systematic uncertainty term is dominated by more fundamental assumptions related to the SED models, etc., which we currently are not able to estimate.

### 5.3. *Blends*

Including blends presents a problem for our source density estimate. In the absence of instrument noise, any blended source which appears red must include at least one genuinely red source. However, such a source may lie below our detection threshold, and hence would not belong in our catalog. Therefore, for a blend of two sources detected at $250\,\mu$m, it is not clear if the source should count as zero, one, or two sources in our density estimate. The probability of the first two can be estimated from models for the color distribution of non-red sources. Furthermore, because the observed number density of sufficiently bright $500\,\mu$m-risers is considerably smaller than non-red sources, it seems reasonable to assume that a red source is much more likely to be blended with a blue source than another red one – which will make the resulting blend bluer, but also may make it bright enough to be selected. This amounts to the assumption that the spatial clustering of bright red sources is not strong enough to compensate for the much larger number of non-red sources, an assumption that we are currently not in a position to test.

Because available models are trained on differential number counts in each band rather than colors (which largely have not been measured), the uncertainty in these predictions is hard to quantify. Therefore, we have chosen to exclude clear blends from our source counts but include their presence as a systematic uncertainty. There are two sources in our catalog that are detected as likely two-component blends in the $250\,\mu$m data (but not in the other two bands): FLS 7 and FLS 23. We are able to make crude estimates of the $S_{250\,\mu\mathrm{m}}$ flux densities of the constituent sources in both cases. Starting with this information, we randomly select single sources that are at least this bright at $250\,\mu$m from a large simulation of the

B11 model, but which are also fainter than the blended source in all bands. We then subtract the fluxes of the simulated source from the blended fluxes of the actual source, use this as an estimate of the flux of the other, red component, and finally determine what fraction of the time the de-blended source would pass our selection criteria.

For FLS 7, we find that 99.8% of the time the de-blended source is sufficiently bright and red to belong in our catalog. For FLS 23, which is significantly fainter, we find that for 110,000 simulated companions, the resulting de-blended source belongs in our catalog zero times. Therefore, we conclude that FLS 7 very likely contains a genuinely red, bright source, while FLS 23 at best contains a red source that is too faint to pass our $D$ selection, and hence does not belong in our catalog.

In order to estimate the systematic uncertainty due to the fact that FLS 7 should be included in our catalog – but with unknown true fluxes and hence unknown efficiency – we compute the efficiency as above but using the ensemble of de-blended model fluxes, and then include 99.8% of that as a positive systematic uncertainty in our final source density estimate. This results in a positive systematic uncertainty of 0.24 deg$^{-2}$ in our FLS source density measurement.

### 5.4. *Source Density*

Combining the results of the purity and efficiency simulations with the input catalog, we finally arrive at our measurement of the source density of red sources in *Herschel* data. One complication is that our S/N requirement of 4 corresponds to slightly different depths in different fields, but in simulations the S/N seems to be a better predictor of the purity than the difference map flux density $D$.

The uncertainties in the efficiencies are quite non-Gaussian. To fold these into our calculation, when computing $N$ from Equation 4, we randomly select an efficiency for each catalog source from our $N_\sigma$ simulation sets, compute $N$ using those values, and then repeat this process several thousand times. We also include the uncertainty in $p$ and the Poisson uncertainties from the number of detected sources in this step. The result is an ensemble of values for each field, drawn from the underlying $N$ distribution. For the FLS field, we find that $N = 4.90^{+1.35}_{-1.47} \, (\text{stat})^{+0.24} \, (\text{sys}) \, \text{deg}^{-2}$ and for Lockman-SWIRE $N = 2.91^{+0.80}_{-0.86} \, (\text{stat}) \, \text{deg}^{-2}$, not including the boosting correction, and where here the systematic uncertainties include only the effect of identified blends. The resulting number density distributions are shown in Figure 12. Given these uncertainties, the two fields are in reasonable agreement, with the difference corresponding to $1.2\,\sigma$. Due to the modest size of our catalogs, Poisson errors dominate our uncertainty budget.

Since the sources in FLS and Lockman-SWIRE completely dominate our catalog (given their much larger areas), and the difference in depth is relatively minor considering the other uncertainties in our computation, we combine the results from these two fields using inverse variance weighting, then apply the boosting correction to give our final estimate of the red-source sky density of $N = 3.27^{+0.67}_{-0.84} \, (\text{stat}) \, \text{deg}^{-2}$ for sources with $S_{500\mu m} \geq 30 \, \text{mJy}$ and $D \geq 23.9 \, \text{mJy}$, with an identified

systematic uncertainty due to partially resolved blends and boosting of $^{+0.06}_{-0.05} \, \text{deg}^{-2}$. The corresponding 95% lower limit is $N > 2.04 \, \text{deg}^{-2}$. Note that these values ignore any potential multiplicity of our sources, which will have to be constrained with interferometric observations. As noted in §4.3, high-resolution observations of a handful of red targets show that the multiplicity fraction appears to be relatively low. This is apparently at odds with the findings of Hodge et al. (2013) – but this requires further study, which will be presented by Clements et al. (in preparation) and Perez-Fournon et al. (in preparation) using a larger sample. The number densities should therefore be interpreted as the number density of sources at the resolution of the SPIRE beam.

We can use the fact that 4/5 of our sources with measured redshifts are at $z > 4$ to estimate the sky density of $z > 4$ DSFGs satisfying our selection. This assumes that the sources with redshifts are representative of our population (see Figure 5), which may not be entirely valid. In particular, FLS 3 and LSW 102 are redder than most of our catalog sources, and most are brighter than the average catalog source at $500\mu m$. Evaluating the effects of this bias requires observations of additional sources. With this caveat in mind, if we denote this fraction by $f_{z>4}$, and assume a flat prior, then, from a simple application of Bayes theorem, the probability distribution for $f_{z>4}$ is given by $P(f_{z>4}) \propto (f_{z>4})^4 (1 - f_{z>4})$. This translates into a mean value of $f_{z>4} = 0.71^{+0.16}_{-0.17}$ (68.3% confidence limits), with a mode of 4/5. The corresponding frequentist confidence interval is $f_{z>4} = 0.48$–$0.96$. Similarly defining the fraction of our sources with $z > 3$ ($f_{z>3}$), we can provide a 95% Bayesian lower limit of $f_{z>3} > 0.61$ ($> 0.83$ at 68.3%). Combining this with the sky density value quoted above, we therefore calculate the number density of $z > 4$ red sources to be $N_{z>4} = 2.37^{+0.75}_{-0.79} \, \text{deg}^{-2}$, and $N_{z>3} > 1.68 \, \text{deg}^{-2}$ (95% lower limit; we do not provide a central confidence interval here because our constraint on $f_{z>3}$ is a lower limit). Note that these results do not make use of photometric redshifts, and in fact the largest contribution to the uncertainty budget in the number of high-$z$ DSFGs selected by our method is due to the small number of sources with spectroscopic redshifts. Clearly the highest priority for future work is to obtain additional redshifts, which will also allow detailed studies of the physical properties of these galaxies. None of these values attempt to correct for non-red DSFGs at high-$z$.

### 6. OTHER RED SOURCES IN THE LITERATURE

There are a number of $500 \, \mu m$-riser sources in the literature with spectroscopic redshifts, the majority of which are at $z > 4$. However, we suspect that this sample suffers from "publication bias": it is highly inhomogeneous, and the fact that these sources were singled out for publication may have been influenced by the fact that they were at high-$z$. Therefore, it is very difficult to draw any quantitative conclusions about how they relate to the population described in this paper. One exception is the recently published South Pole Telescope (SPT) selected sample of bright, lensed DSFGs of Vieira et al. (2013). Here the sources were selected at 1.4 mm in a uniform fashion, but SPIRE observations reveal that most of those at $z > 4$ are $500 \, \mu m$-risers. In this section we
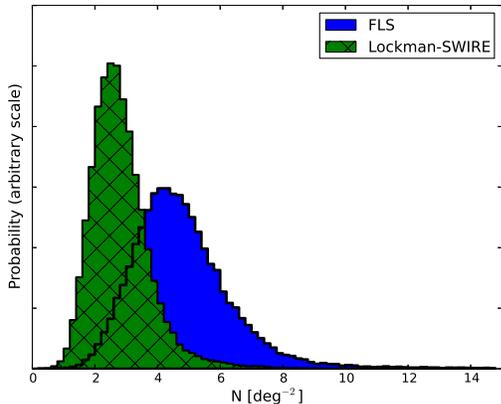
**Figure 12.** Estimated red source density per $deg^2$ for our two large fields, FLS (solid blue) and Lockman-SWIRE (hatched green), including all identified statistical uncertainties. The smaller fields (Lockman-North, Lockman-East, and GOODS-N) are not shown because of their significantly different depths, and because their limited size (a total of 1.1 $deg^2$ compared with the 20.3 $deg^2$ of the fields shown) means that they make very little contribution to our final catalogs.

summarize information about red literature sources, particularly the SPT sample, which is discussed at the end of the section.

Combes et al. (2012) discovered a bright ($S_{500\mu m} > 200$ mJy) $500\,\mu m$-riser at $z = 5.2$ highly magnified by the cluster Abell 773. Similarly, Cox et al. (2011) discusses a strongly-lensed $500\,\mu m$-riser with $z = 4.24$. Both sources would be easily detected by our method, and in fact were selected using SPIRE data. Swinbank et al. (2012) describes two sources at $z = 4.4$ with redshifts serendipitously measured during a high-resolution continuum mapping program in GOODS-S. Examination of the deep HerMES GOODS-S map shows that both sources are $500\,\mu m$-risers, but are fainter than our $S_{500\mu m}$ cutoff.

There are also a number of known $z > 4$ DSFGs detected at longer wavelengths ($> 850\,\mu m$) that are too faint to be detected in SPIRE data (irrespective of our selection technique), such as the $z = 4.8$ source described by Coppin et al. (2009), or the one at $z = 5.2$ from Walter et al. (2012). Perhaps more interestingly, there are at least two examples of $z > 4$ DSFGs that are detected in the SPIRE bands, but have $S_{350\mu m} > S_{500\mu m}$: AzTEC-3 ($z = 5.3$ Capak et al. 2011; Riechers et al. 2010), and GN20/20.2 ($z = 4$ Pope et al. 2005; Daddi et al. 2009). A reasonable inference is that some $z > 4$ DSFGs have warmer dust temperatures, and hence are not selected by our method.

Casey et al. (2012) performed an optical redshift survey of *Herschel*-selected sources, some of which were $500\,\mu m$-risers. In order to be included in this sample, a $24\,\mu m$ or radio counterpart was required, which is expected to bias against high-$z$ sources. Furthermore, the spectroscopic success rate also has a redshift dependence, and it is possible that the counterpart-identification process may have a higher mis-identification rate for high-$z$ sources. Together, these effects make it somewhat difficult to compare this sample to ours. Using the flux densities derived as part of the counterpart identification process, there are two sources that would satisfy our se-

lection criteria. One of those is clearly an error – there is no detected source in any of the SPIRE bands. Analysis of the maps at the location of the other source shows that it would barely fail our selection criteria in $S_{500\mu m}$ and $D$, but that the source appears to be red. It has a optical redshift of 0.47. It is possible that this is a lensed source, and that the redshift is that of the foreground lens; sub-mm/mm interferometry would be required to be sure.

Vieira et al. (2013); Weiß et al. (2013) present the results of a redshift survey of SPT-selected DSFGs from 1300 $deg^2$ of observations. The selection requirements are $S_{1.4\,mm} > 20\,mJy$ and that the 1.4 mm vs. 2 mm flux density ratio is dust-like rather than synchrotron-like, with additional screening against $z < 0.03$ candidates and radio loud sources. They obtained secure, multi-line spectroscopic redshifts, primarily from the $^{12}CO$ ladder, for 19 sources, as well as single- or low signal-to-noise multi-line, redshifts for an additional six objects. Furthermore, they obtained *Herschel*/SPIRE observations of this sample. By selection, these sources are significantly brighter than the sample presented here, and therefore, as expected from models (e.g., Negrello et al. 2007), follow up reveals that all of these sources are strongly lensed. This is a well defined sample with SPIRE coverage, and hence is useful to compare with our study.

While the authors argue that the redshifts of several of the SPT sources with single line detections can be inferred from the shape of the thermal SED (by assuming "typical" dust temperatures) or the lack of additional lines, the possibility of weak CO lines or unusual dust temperatures – examples of which are known from the literature (e.g., Conley et al. 2011; Casey et al. 2012) – remains. Therefore, here we consider only SPT sources with secure, multi-line spectroscopic redshifts. With this requirement, the band coverage of the redshift search (primarily from 84 to 115 GHz) imposes a somewhat complicated redshift selection effect which favors $z > 3$ – that is, for sources at $z < 3$ only single lines could be detected in most cases at the depth of their observations, resulting in ambiguous redshifts. For some of the SPT sources this is alleviated by the presence of additional follow-up observations at other frequencies. Furthermore, the addition of the 1.4 mm flux selection clearly introduces a relative selection bias between the SPT sources and the sample presented here, even for SPT sources that are also $500\,\mu m$-risers – although the amount can not be estimated without adding strong assumptions about the underlying population. Detailed lens models are available for four of the SPT sources, but if we assume lens magnification factors of 5–25, as suggested by those four sources, then, on average, the SPT population is intrinsically less luminous than our sample, assuming that our sources are not highly lensed on average. Our method is substantially more efficient at selecting high-$z$ sources (in terms of the overall fraction of sources at high-$z$ as well as the source density), but, because they are strongly lensed, the SPT sources are much easier to study in detail.

Ignoring these complications, seven of the 10 SPT sources with $z > 4$ are $500\,\mu m$-risers, while the other three are brightest at $350\,\mu m$. One of these is clearly not red in the SPIRE bands, while the other two have $S_{500\mu m} \simeq S_{350\mu m}$ to within $1\sigma$. In addition, there are

three SPT $500\,\mu$m-risers with $3 < z < 4$ and an additional four $500\,\mu$m-risers with single line redshifts which we exclude from this discussion. This suggests that red SPIRE colors are a relatively efficient and complete method of finding 1.4 mm-selected sources at $z > 4$.

## 7. INTERPRETATION

### 7.1. *Comparison of Observed Number Density with Galaxy Evolution Models*

To compare the number of observed bright and red SPIRE sources to the number predicted by pre-existing models, we consulted models by Béthermin et al. (2011, 2012); Fernandez-Conde et al. (2008); Franceschini et al. (2010); Le Borgne et al. (2009); Valiante et al. (2009); Xu et al. (2001) using mock catalogs. The comparisons are summarized in Table 6 and discussed in detail in this section. Generally, these models are not physically motivated, and are developed based on the properties of lower-$z$ DSFGs. The goals of this comparison are to test if the properties of the DSFG population can be simply extrapolated from $z \sim 2$, or if additional evolution is required, and how well these models can be used to plan for future surveys of high-$z$ DSFGs.

For the Fernandez-Conde et al. (2008) simulations, which are based on Lagache et al. (2004), we used a simulated data set covering $5.2\,\mathrm{deg}^2$ and with a bias parameter 1.5. For the Le Borgne et al. (2009) model, we used a mock catalog covering $10\,\mathrm{deg}^2$ and containing 2 million galaxies. In both cases we found zero sources satisfying our selection criteria. We can therefore conclude that the predictions of these models for the number of red sources are overwhelmingly ruled out by our observations.

The other models predict some red sources, but in general they do not match the properties of our observed population. A $93\,\mathrm{deg}^2$ simulation of the B11 model, containing 20 million galaxies, predicts $1.1\,\mathrm{deg}^{-2}$ red sources satisfying our selection criteria, but only $0.05\,\mathrm{deg}^{-2}$ lie at $z > 3$ and 0 at $z > 4$, corresponding to a 95% upper limit of $< 0.03\,\mathrm{deg}^{-2}$. Hence, this model over-predicts the number of low-$z$ sources, and significantly under-predicts the number of high-$z$ ones. The Valiante et al. (2009) model, which is based on observed galaxies with luminosities up to $10^{12.8}\,\mathrm{L}_\odot$ and incorporates a correlation of luminosity and mean dust temperature, predicts 15 sources satisfying our selection criteria in a simulated area of $10\,\mathrm{deg}^2$ and containing 8.2 million galaxies. However, zero of these galaxies are at $z > 4$, and only three are at $z > 3$. Furthermore, they have significantly colder dust temperatures ($\sim 30\,\mathrm{K}$) than our sources with known redshifts.

The Franceschini et al. (2010) model over-predicts the number of sources that meet our observational selection criterion, predicting $10\,\mathrm{deg}^{-2}$. However, their predictions for the number of sources at high-$z$ are closer to our limits: $1.2\,\mathrm{deg}^{-2}$ at $z > 4$ and $3.4\,\mathrm{deg}^{-2}$ at $z > 3$. Thus, their prediction for $z > 4$ is only lower than the observed number by a factor of 2 ($1.5\sigma$), although they also predict a large number of red sources at lower $z$ that are not consistent with observations.

For the Xu et al. (2001) models, we used mock catalogs covering $10\,\mathrm{deg}^2$ which have been updated to better match the Spitzer number counts. This substantially over-predicts the number density of red sources

at $12\,\mathrm{deg}^{-2}$. However, the predicted number of $z > 4$ sources is much smaller, $0.08\,\mathrm{deg}^{-2}$, which is strongly ruled out. Again, this model also predicts a very large number of red sources at lower $z$ which are not seen in the data. Inspection of these sources show that most are classified as having "AGN" rather than "starburst" templates. Closer inspection of the templates that meet our source selection criteria indicate that the models may have poor applicability for these types of sources. For example, the template within the model catalogs which most often passes the selection criteria is based on the $10^{11.8}\,\mathrm{L}_\odot$ galaxy Mrk 0309, which is assumed to have a dust temperature of $\sim 22\,\mathrm{K}$ (for $\beta = 1.5$), despite being scaled up by a factor of 5 in luminosity for the catalogs, and despite having no published measurements for the template fit at $\lambda > 100\,\mu$m. Galaxies with luminosity of $10^{12.5}\,\mathrm{L}_\odot$ and average dust temperature $22\,\mathrm{K}$ may exist, but the Mrk 0309-based template is not yet a convincing example of one.

The B12 models fare considerably better. We generated catalogs representing $200\,\mathrm{deg}^2$, and found a predicted red source density of $0.58\,\mathrm{deg}^{-2}$. Furthermore, all of the red sources predicted by this model are at $z > 3$, with $0.49\,\mathrm{deg}^{-2}$ at $z > 4$. Folding in the efficiency distribution, and including the predicted contamination rate by "orange" sources, the B12 model predicts that we should select 14.7 sources over our fields, compared with the 38 actually found. This corresponds to a $P$ value of $3 \times 10^{-7}$, so formally this model is still excluded at very high significance. However, it is clear that it is much closer to our observations than the other models, and it is worth attempting to understand why this is the case. There are two primary reasons. First, the B12 predicts more high-$z$, luminous DSFGs than many of the other models – although not, for example, the B11 model. Second, the SED templates for luminous DSFGs are redder, on average, than for most of the other models – this is the most important difference in comparison with the B11 model. In addition, the B12 model implements some scatter in the templates for a fixed $z$ and luminosity, which most of the other models do not. However, this seems to have a relatively modest effect – doubling the scatter increases the predicted source density by about 25%, but entirely by adding bright $z < 3$ red sources which, so far, have not been observed. Furthermore, it disturbs the agreement of this model with the observed far-IR/sub-mm monochromatic differential number counts. The cumulative number counts for the B11 and B12 models, compared with our observations, are shown in Figure 13.

One possibility for improving the agreement of these models with observations is that there may be significantly more strong lensing at high redshifts than expected. Here we explore how much *more* lensing would be required to match our observations with current population models using the B11 model. The B11 model already contains lensing, but we can consider the effects of modifying this prescription. If we substitute the lensing model of Wardlow et al. (2013), the number of red sources is significantly increased to $1.4\,\mathrm{deg}^{-2}$. However, most of these are at $z < 2$; the number densities at $z > 3$ and $z > 4$ are increased to 0.3 and $0.2\,\mathrm{deg}^{-2}$, respectively. This is a step in the right direction, but is clearly
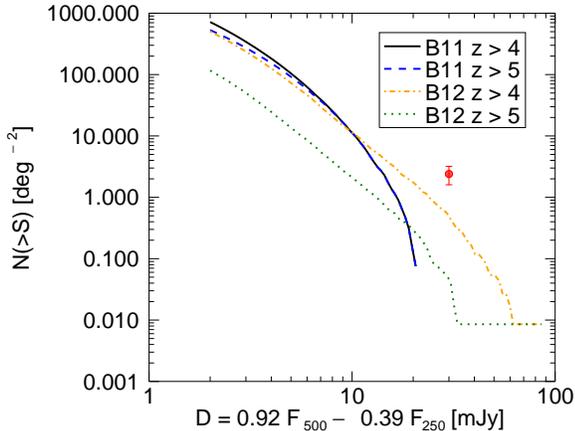
**Figure 13.** The cumulative number counts (red DSFGs brighter than a specified flux density in the difference map, $D$) for the B11 and B12 models, based on the simulations discussed in the text. Shown, for comparison, is our measurement of the number density of $z > 4$ red DSFGs from §5.4.

still inconsistent with our observations. Furthermore, the observed flux density distribution clearly does not match our population – the number of $S_{500\mu m} > 50$ mJy sources at $z > 3$ is only $0.05$ deg$^{-2}$. The five sources with redshifts that we have, even ignoring efficiency corrections, already rule this out at $> 99.8\%$.

Next we consider modifying the Wardlow et al. (2013) lensing model. If we scale up all lensing probabilities above $\mu = 1.5$ by a constant factor, we find that we must increase them by $20\times$ in order to match our source density at $z > 3$, which is extremely unlikely. Rather than increasing the frequency of large magnifications, which does not seem to work, a different way to look at the problem is to impose a minimum magnification floor at $z > 3$ on the model. We can not do so for all sources, because for physical reasons the mean magnification over all lines of sight must be one to any redshift. However, because large magnifications are rare in any such model, a reasonable approach is to adjust the Wardlow et al. (2013) model by setting $P(\mu) = 0.5$ between $\mu = 1$ and $\mu = \mu_{low}$ (with the probability distribution above $\mu_{low}$ unaltered), and explore how large $\mu_{low}$ must be to reconcile models with observations. Carrying out this procedure, we find that, for the B11 model, we require $\mu_{low} = 2.1$. In other words, *half* of all sight-lines to $z > 3$ must be magnified by a factor of two or more. This is not realistic. Applying the same analysis to the B12 model does not change much – to match observations either the high-magnification tail must be increased by $15\times$, or half of all sight-lines must be magnified by more than $\mu = 1.8$.

As discussed in §5.4, our measured number density is effectively at the resolution of SPIRE ($> 18''$). While our counts are corrected for blends with non-red objects, if our sources have a high multiplicity (i.e., all of our catalog objects are in fact composed of two or more red sources), then this will affect the (dis-)agreement with models. The best way to investigate this topic is to obtain higher-resolution (interferometric) sub-mm/mm observations. However, because the above phenomenological models are trained to match observed number counts that have the same resolution issues, in order for multi-

plicity to bring their predictions in agreement with our observations it must be a strong function of redshift such that it affects our sources much more than lower-$z$ DSFGs. This does not seem particularly likely, but it can not be ruled out at this point. For example, if luminous DSFGs at all redshifts are actually comprised of two sources too close to each other to be resolved, then, in order to maintain agreement with the overall observed number counts of all sources, the number of predicted red (but now undetectably blended) sources at SPIRE resolutions would not change.

Overall, pre-existing models significantly under-predict the number of high-$z$, red sources we detect. The one exception is the model of Franceschini et al. (2010), which is a reasonable match for the number of high-$z$ galaxies detected by our technique, but also predicts a very numerous population of lower-$z$ red sources highly inconsistent with *Herschel* observations. Of the models that do not share this issue, the B12 model performs the best, although it is still ruled out at high significance. In any case, this comparison suggests that there must be additional evolution in the DSFG population at $z > 3$ beyond that predicted by simple extrapolations from lower redshift. It seems certain that gravitational lensing will play a role in reconciling population models with observations, but for the current generation of such models the required amount of lensing is not reasonable.

### 7.2. Overlap of Our Red SPIRE Sample with Millimeter-Selected Galaxies

Given our selection criterion of monotonically rising spectra with increasing wavelength in the SPIRE bands, we would expect the selected objects to be strong emitters at $\lambda \approx 1$ mm. This is now demonstrated for a subset of the sample, as discussed in §4. In this section, we examine the reverse implication using mm-wave observations that cover a small fraction of the HerMES fields: do mm-selected sources have properties similar to the red SPIRE sources in this paper?

With two exceptions[44], existing $\lambda \approx 1$ mm "blind" surveys sensitive enough to detect significant numbers of high-redshift galaxies cover areas less than 1 deg$^2$, and measure a population with $\sim 100\times$ the surface density of our red SPIRE galaxies. Therefore, by virtue of observational selection, we can not have good correspondence with these surveys. It is reasonable to expect that the degree-sized mm surveys will uncover objects that are typically fainter at far-IR through millimeter wavelengths and likely have lower luminosity. The comparison with lensed, mm-selected SPT sources (which also have SPIRE observations) was already presented in §6.

Within the SPIRE SDP fields discussed in this paper, the AzTEC 1.1 mm survey of Lockman Hole East (Austermann et al. 2010) covers the largest area with $\sim$1 mJy depth. The AzTEC survey produced a primary catalog of 43 sources with $4\sigma$ statistical significance over an area of $0.3$ deg$^2$. None of these correspond to red SPIRE sources cataloged in Table 2. However, all 17 of the AzTEC sources with greater than $5\sigma$

---

[44] The South Pole Telescope (Mocanu et al. 2013) and Atacama Cosmology Telescope (Marsden et al. 2013) surveys; due to their large areas, however, these are effectively much shallower than the HerMES survey.

**Table 6**
Predicted number of red SPIRE sources

| Model | Predicted Density [deg$^{-2}$] | | | Reference |
| | Red | Red $z > 3$ | Red $z > 4$ | |
|---|---|---|---|---|
| Béthermin 11 | 1.1 | 0.05 | < 0.03 | Béthermin et al. (2011); B11 |
| Béthermin 12 | 0.58 | 0.58 | 0.49 | Béthermin et al. (2012); B12 |
| F.-Conde | < 0.6 | < 0.6 | < 0.6 | Fernandez-Conde et al. (2008) |
| LeBorgne | < 0.3 | < 0.3 | < 0.3 | Le Borgne et al. (2009) |
| Valiante | 1.5 | 0.2 | < 0.3 | Valiante et al. (2009) |
| Franceschini | 10 | 3.4 | 1.2 | Franceschini et al. (2010) |
| Xu | 12 | 0.34 | 0.08 | Xu et al. (2001) |
| Observed | $3.27^{+0.67}_{-0.84}$ | > 1.68 (95%) | $2.37^{+0.75}_{-0.79}$ | This work |

**Note**. — Comparison of the prediction of various pre-existing models with the observed number of red sources satisfying our detection criteria ($D \geq 23.9$ mJy, $S_{500\mu m} \geq 30$ mJy, $S_{500\mu m} \geq S_{350\mu m} \geq S_{250\mu m}$). The upper limits, which are provided when no such sources were generated in our simulations, are the 95% one-sided frequentist limits, and are set by the sky area simulated for each model. The number of red sources at $z > 3$ and $z > 4$ are based on combining the measured sky density with the observation that 4/5 of our sources with redshifts are at $z > 4$, and 5/5 at $z > 3$.

statistical significance are associated with clear SPIRE sources and positive peaks in the difference image $D$. These sources range in 1.1 mm brightness from 3.6 to 6.6 mJy (deboosted), with a mean of 4.6 mJy. We stacked the SPIRE 50″-resolution images at the positions of the 17 AzTEC sources. The stacked mean values of $S_{250\mu m}$, $S_{350\mu m}$, $S_{500\mu m}$ and $D$ are 30.1, 34.1, 25.7, and 11.4 mJy, respectively. Collectively, then, these mm-selected sources peak at shorter far-IR wavelengths than the red sample in this paper, and they are a factor of $\sim 1.3$ fainter in the far-IR.

Only one source – #13 – among the 17 AzTEC $5\sigma$ sources has a SPIRE counterpart which meets our redness criterion, but not our brightness criterion. In matched 50″ beams, it has flux densities $S_{250\mu m}$, $S_{350\mu m}$, $S_{500\mu m}$ of 12.4, 25.8, 29.0 mJy, respectively. A tentative photometric redshift of 2.1 – ironically below the median for the sample – was assigned to source 13 by the AzTEC team (Michałowski et al. 2012) based on a radio and 24 $\mu$m counterpart. However, the radio and 24 $\mu$m source appear to be offset by similar distance and direction from both the AzTEC and SPIRE source, so may not be physically associated.

### 7.3. Contribution of Red Sources to Far-IR Background

Using our completeness and purity simulations, it is simple to estimate the contribution of sources selected by our method to the cosmic far-infrared background (CIB) at 500 $\mu$m by weighting the number density calculation by $S_{500\mu m}$. Carrying out this procedure, we find for the FLS field a value of $0.66 \pm 0.20$ kJy sr$^{-1}$, and for Lockman-SWIRE $0.38 \pm 0.10$ kJy sr$^{-1}$, where the uncertainty in the observed fluxes and Poisson fluctuations (which account for $\sim 2/3$ of the error budget) are included, but not the uncertainty in the SPIRE calibration. These differ by $1.3\sigma$, and hence are consistent. Compared with the FIRAS measurement of $0.39 \pm 0.10$ MJy sr$^{-1}$ (Fixsen et al. 1998), the red sources with $S_{500\mu m} > 30$ mJy account for only 0.1–0.2% of the background. Note that these only represent the intrinsically most luminous high-$z$ DSFGs, and non-red sources at these redshifts are not included, but, assuming that the luminosity function for DSFGs has a similar shape at $z > 3$ as it does at $z \sim 2$, 500 $\mu$m-risers probably do not account for more than a few percent of the CIB at 500 $\mu$m.

### 7.4. Photometric Redshifts

Up until this point in the paper, we have tried to avoid any analysis which requires photometric redshifts, but they are required in order to estimate the contribution of our sources to the star formation history of the Universe. We have firm spectroscopic redshifts for only five of the galaxies in our sample. Without precise interferometric positions, we are limited to the properties of the thermal dust SEDs to derive photo-$z$s. Because modified blackbody models are perfectly degenerate in $T_d / (1 + z)$ and $\lambda_0 (1 + z)$, deriving photo-$z$s from these data essentially requires assuming a prior on the rest frame values of these parameters. Here we attempt to derive a crude estimate of the redshift distribution of our population using such a prior. Note that here we are not making use of the priors discussed in §3 in any way.

Instead of working with the dust temperature $T_d$, which is rather indirectly constrained by the data, we use the wavelength at which $S_\nu$ peaks, $\lambda_{max}$, for each source. We construct a prior for the rest-frame $\lambda_{max}$ by following the approach of Greve et al. (2012): collect a comparison sample of DSFGs (with precise spectroscopic redshifts and well constrained thermal SEDs), and analyze them using the same modified blackbody model. If the (observer frame) peak wavelength of each red source is $\lambda_{max}^S$, and the (rest frame) peak wavelength of each comparison source is $\lambda_{max}^C$, then the photometric redshift estimate $z_p$ for that red source from that comparison is $1 + z_p = \lambda_{max}^S / \lambda_{max}^C$. Because our SED analysis is based on MCMC methods, we can also easily include measurement uncertainties in each $\lambda_{max}^{\{C,S\}}$.

The results depend sensitively on the comparison sample. Ideally, this sample would be selected in exactly the same manner (adjusting for redshift) as our red sources – but no such sample is currently available. We considered several possible compilations, evaluating them based on how well they predict the redshifts of a test sample consisting of our five red sources with spectroscopic redshifts as well as the red sources from Combes et al. (2012) and Cox et al. (2011), both of which were discovered in *Herschel*/SPIRE observations and which would clearly be selected using our method. We do not include the SPT red sources in our test sample because it is not clear how the 1.4 mm selection will bias the selection relative to ours. Magnelli et al. (2012) present a detailed study of "classic SMGs" at $z \sim 2.4$ selected based on longer wavelength

$(850\,\mu\mathrm{m}$–$1.2\,\mathrm{mm})$ observations, and with redshifts generally determined on the basis of radio cross-identifications, using the same SED model. The longer wavelength selection is expected to bias this sample relative to ours towards colder sources, and hence towards lower redshifts for fixed SPIRE colors. Indeed, analysis of this sample gives $z_{\mathrm{p}} \sim 2$ for our seven test sources ($z_{\mathrm{p}} \sim 3$ for FLS 3), which can be ruled out at very high significance, as $6/7$ are at $z > 4$. Therefore, as a comparison sample this does a very poor job predicting the redshifts of our sources – so poorly, in fact, that it is not possible to re-weight it to provide a good estimate. The same is true, but to a lesser extent, for the SPT sample of Vieira et al. (2013): the sources are colder, and hence under-predict the redshifts of our test sample.

The Casey et al. (2012) study discussed in §6 presents redshifts for a large sample of *Herschel*-selected DSFGs, with the additional requirement that they be detected in *Spitzer* $24\,\mu\mathrm{m}$ or radio observations. While that paper uses a somewhat different SED model, they also present $\lambda_{\max}$ measurements. At the typical $L_{\mathrm{IR}}$ of our sources ($\sim 10^{13}\,\mathrm{L}_{\odot}$), this predicts $\langle z_{\mathrm{p}} \rangle \sim 9$, which is again strongly ruled out. This may be the result of selection biases in the $\lambda_{\max}$-$L_{\mathrm{IR}}$ relation of the Casey et al. (2012) sample. If we instead select $S_{500\mu m} > S_{350\mu m} > S_{250\mu m}$ sources – now dropping the minimum flux requirements to $S_{500\mu m} > 10$ mJy in order to increase the comparison sample size (to 19 sources) – we find $\langle z_{\mathrm{p}} \rangle = 6.3$ for the comparison sample (excluding FLS 3), an improvement, but again strongly ruled out. These sources have similar colors as those of our red sample, so this is somewhat surprising – the $24\,\mu\mathrm{m}$/ radio and optical spectroscopic success requirements are expected to bias this sample towards lower $z$, increasing the rest-frame $\lambda_{\max}$ values, which would lead to an under-prediction of $z_{\mathrm{p}}$ for our test sources rather than the observed over-prediction. In any case, this does not seem to be a good comparison sample for our purposes.

Finally, we consider the compilation of well-observed *Herschel*-selected lensed sources of Greve et al. (2012), also at $z \sim 2$ (which these authors used to make photo-$z$ estimates for $1.4\,\mathrm{mm}$-selected SPT sources). They fit the photometry of the lensed sources using a similar SED model, but holding $\beta$ and $\lambda_0\,(1+z)$ fixed. Because these sources are generally quite well observed, we re-fit this sample using our model but without fixing these parameters (or using priors), excluding the few sources where the data quality was insufficient to constrain such a fit. Comparison with our test sample gives $\langle 1 + z_{\mathrm{p}} \rangle / \langle 1 + z_{\mathrm{spec}} \rangle = 0.93 \pm 0.08$, much better than the other comparison samples. These highly magnified sources almost certainly probe a different (fainter) luminosity range than our red sources. This may result in some bias in the photo-$z$s; for example, if dust temperature increases with luminosity, we would expect the lower-$z$ lensed galaxies to peak at longer rest-frame wavelengths than our red sources, and hence under-predict the redshifts. However, we do not apply any correction, since the derived photo-$z$ values are consistent overall with the spectroscopic redshifts of our test sample. We further supplement this collection by including the fits to FLS 1, FLS 3, FLS 5, and LSW 20 as in §4.7, resulting in a final comparison sample of 19 DSFGs.

Applying this effective prior to the $\lambda_{\max}$ values derived
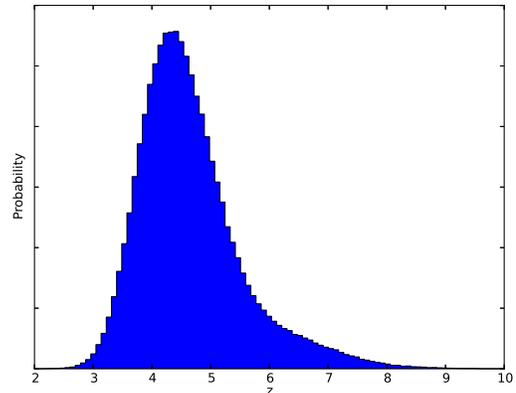


**Figure 14.** The photo-$z$ distribution of our sample using the SED prior discussed in the text.

in §3 results in the population distribution given in Figure 14. This gives $\langle z_{\mathrm{p}} \rangle = 4.7$ with a one sigma range of $\pm 0.9$, and with 20% of the population at $z < 4$ – consistent with the existence of LSW 20 at $z = 3.4$ in our test sample. The tail to higher redshift is due to the fact that, for the redder sources in our sample, the upper limit on $\lambda_{\max}$ is not as well constrained as the lower limit, although the existence of FLS 3 at $z = 6.34$ demonstrates that there are at least some $z > 6$ DSFGs. Adding more longer-$\lambda$ observations would help constrain this tail.

### 7.5. Contribution of these Sources to high-z Star Formation

At this time, the paucity of spectroscopic redshifts of our sources prevents a precise calculation of their contribution to the star formation history of the Universe. However, we can extend the photometric redshift model discussed in §7.4 to form a rough estimate. Each of the comparison sample sources has a well determined thermal SED, so in addition to using randomly sampled $\lambda_{\max}^C$ values, we also take the corresponding values of the SED parameters ($T_{\mathrm{d}}$, $\beta$, etc.), redshifting that SED to the corresponding $z_{\mathrm{p}}$ of the catalog source, and scaling it to match the observed $500\,\mu\mathrm{m}$ flux density. For this calculation we must also correct for the selection efficiency and purity, as discussed in §5, so for each $z_{\mathrm{p}}$, $L_{\mathrm{IR}}$ pair we also associate a randomly drawn $\epsilon$ and $p$ appropriate to that source. Doing this once for each source in our catalog provides a single simulation of our red source sample. We then bin the simulated sources by $z_{\mathrm{p}}$ into two broad bins ($z_{\mathrm{p}} =$4–5 and $z_{\mathrm{p}} =$5–6), add up the total $L_{\mathrm{IR}}$ in each bin, counting each catalog source as $p/\epsilon A$ sources per $\mathrm{deg}^2$, where $A$ is the area of the field that that source comes from. For those sources in our main survey area with spectroscopic redshifts (FLS 1, FLS 3, FLS 5, and LSW 20) we instead sample $L_{\mathrm{IR}}$ directly from their SED fits (§4.7), hence excluding both FLS 3 and LSW 20 from our calculation as they lie outside both redshift bins.

We then divide the total $L_{\mathrm{IR}}$ in each bin by the comoving volume per $\mathrm{deg}^2$, and convert to a star formation rate density (SFRD) using the Kennicutt (1998) conversion. By repeating this procedure 5000 times, and folding in Poisson noise due to the limited sample size, we can estimate the uncertainty in the SFRD from these sources, deriving values of $(1.5 \pm 0.5) \times 10^{-3}$ and $(8.6 \pm 4.9) \times 10^{-4}$

$M_\odot \, yr^{-1} \, Mpc^{-3}$ at $4 \leq z < 5$ and $5 \leq z < 6$, respectively (Figure 15). About half of the uncertainty budget in the lower bin and the majority in the higher bin arises from Poisson noise. Note that we make no attempt to correct for non-red DSFGs at these redshifts, nor for sources fainter than our detection limit. These values thus represent only the contribution to the SFRD from the most luminous, heavily obscured far-IR galaxies.

This discussion assumes that AGN activity is not a major contributor to the far-IR luminosity of our sources, as is thought to be the case for lower-$z$ DSFGs (Alexander et al. 2005). Unfortunately, given the high redshift, extreme obscuration, and modest source density of our sources, obtaining sufficiently deep X-ray data for even a small fraction of our catalog would be prohibitively expensive. However, we note that the closest X-ray source to GOODSN 8 in the 2 Msec *Chandra* Deep Field North catalog (Alexander et al. 2003) is $18''$ away, which, given our positional uncertainties, is unlikely to be related.

If we assume that the *shape* of the DSFG luminosity function does not evolve from $z \sim 2$ to $z \sim 5$ (which is almost certainly not true in detail, and may not even be a good approximation), then we can correct for the presence of fainter starbursts. Further assuming that our $z > 4$ targets have $L_{IR} > 10^{13} \, L_\odot$, based on the results of §4.7, and using the B11 luminosity function [45], the contribution to the SFRD from red, $z > 4$ DSFGs is similar to the extinction-corrected, UV-inferred SFRD at the same redshifts of Bouwens et al. (2007), as shown in Figure 15. Using the B12 luminosity function increases this by a further factor of three. Again, we have not made any attempt to include non-red $z > 4$ DSFGs. Furthermore, the overall SFRD for these luminosity functions is dominated by sources with $L_{IR} \sim 10^{12} \, L_\odot$, which are too obscured to be detected in the rest-frame UV even in deep *HST* observations. Clearly, the exact values should not be taken too seriously, but they do suggest that rest-frame UV based estimates of the star formation history of the Universe may be missing a significant component of the SFRD, even after corrections for extinction. Determining whether or not this is the case will require further observations – with the goals of both increasing the number of red sources with spectroscopic redshifts, and extending the search to fainter sources.

## 8. CONCLUSIONS

We have presented a method for selecting candidate high-$z$ dusty star-forming galaxies using *Herschel*/SPIRE colors, and provided a catalog of such sources selected from the first 21.4 deg$^2$ of data from the HerMES project.

- The number density of red $S_{500\mu m} \geq 30, D = 0.92 S_{500\mu m} - 0.39 S_{250\mu m} \geq 23.9$ mJy sources in confusion limited SPIRE maps is $\sim 2 \, deg^{-2}$. After modeling for selection efficiency and contamination, this implies an underlying number density of $3.3^{+0.7}_{-0.8} \, deg^{-2}$. The 95% lower limit is 2.0 deg$^{-2}$.

- We have obtained redshifts for five targets selected

[45] See Figure 11 of B11, noting that the only change in the shape from $z = 3$ to 5 is an increase in $L_\star$ by 6%.
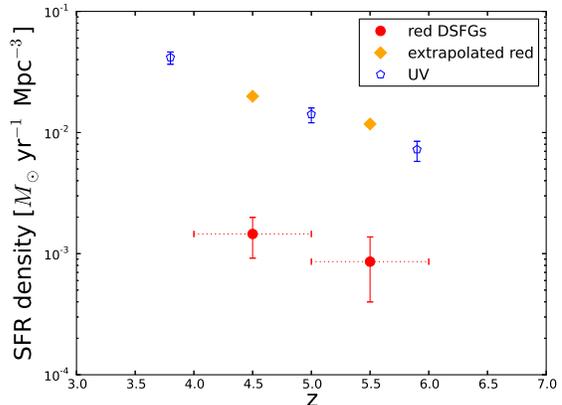


**Figure 15.** Estimated contribution of our $500 \, \mu$m-riser selected DSFGs to the star formation rate density at $z = 4$–6 (red circles). No correction is made for fainter sources, or for DSFGs in this redshift range that are not red in the SPIRE bands. The horizontal bars reflect the bin size, and are not uncertainties. The orange diamonds show the red points corrected for fainter sources using the B11 luminosity function. For comparison, the blue pentagons are the extinction corrected values derived from rest-frame UV *HST* surveys for sources brighter than $0.3L_\star$ (Bouwens et al. 2007); these include significantly lower luminosity sources than the red points.

using our method. They range from $z = 3.4$ to 6.3, with 4/5 at $z > 4$.

- SED modeling of the sources with redshifts shows that they correspond to the luminous tip of the lower-$z$ DSFG luminosity function, with typical $L_{IR} > 10^{13} \, L_\odot$.

- Combining the measured redshifts with the source density, we estimate the number of red, luminous $z > 4$ DSFGs to be $2.4 \pm 0.8 \, deg^{-2}$; the largest uncertainty is due to the small number of sources with secure spectroscopic redshifts.

- The number of such high-$z$ DSFGs is significantly higher than the predictions of existing population models. While gravitational lensing clearly has a role to play in understanding this population, the amount required to reproduce observations with current population models appears to be unrealistic.

- Using a photo-$z$ model based on the properties of lower-$z$, lensed, *Herschel*-selected DSFGs, we estimate $\langle z \rangle \sim 4.7$ for our population.

- Extending this model to predict the contribution of red sources satisfying our selection criteria to the star formation rate density, we find $\sim 10^{-3} \, M_\odot \, yr^{-1} \, Mpc^{-3}$ at $z \sim 5$. This is significantly lower than the total inferred SFRD at these redshifts – but these represent only the tip of the luminosity function.

- If the ratio between the most luminous sources and the rest of the population is similar at $z > 4$ to that for lower-$z$ DSFGs, then DSFGs may contribute a similar amount to the overall star formation density

at these redshifts as the extinction corrected, rest-frame UV measurements – which do not account for such highly extinguished systems.

This sample represents less than 1/5 of the 110 deg$^2$ of the main HerMES survey, which reaches similar depths, and an even smaller fraction of the 300 deg$^2$ of the shallower HeLMS companion survey (Oliver et al. 2012). The number density of sources selected by our method should be a good description of all but the deepest (e.g., GOODS-N) confusion limited SPIRE maps, although we are working to improve this by using more optimal filtering. In shallower surveys, such as HeLMS or H-ATLAS (Eales et al. 2010), the number density will be lower. For example, to a depth of 50 mJy at $500\,\mu$m, the number density (without purity or completeness corrections) is $\sim 0.5$ deg$^{-2}$, about $4\times$ less, based on our catalogs. Follow-up of our sources is ongoing at a wide range of facilities. Obtaining more redshifts is the highest priority for future studies.

# APPENDIX

## MODIFIED BLACKBODY SED FITS

Here we discuss the details of our modified blackbody fits to the thermal SEDs of our sources. The basic model is given by Equation 3, and is written in terms of the blackbody function (through the dust temperature $T_{\rm d}$), the dust properties ($\beta$ and $\lambda_0$), and the overall normalization ($\Omega$). Note that using $\Omega$ directly is a poor choice for fitting purposes because it is extremely degenerate with $T_d$, so instead we use the observer frame flux density at $500\,\mu$m as the normalization parameter. Tests show that this parameterization is much better behaved. We use flat priors over all model parameters.

We have developed code to fit this model to SED data using an Markov Chain Monte Carlo (MCMC) method. An earlier version of this code was also used by Riechers et al. (2013) to analyze the photometry of FLS 3, and we have made it freely available[46]. We make use of the parallelized affine-invariant MCMC `python` module `emcee` (Foreman-Mackey et al. 2013), which in practice has better convergence properties than the more commonly used Metropolis-Hastings method. We check convergence of our chains by requiring that the autocorrelation length for each model parameter is several times less than the number of steps taken during an initial burn-in stage (which are then discarded).

Compared with the version of this code used by Riechers et al. (2013), several improvements have been made. First, we have added the ability to impose upper and lower limits as well as Gaussian priors on the model parameters. These

---

[46] https://github.com/aconley/mbb_emcee.

additions are useful for analyzing poorly constrained data, such as when we consider fits to only the SPIRE photometry in §3. Second, instead of treating the instrument response as a delta function in wavelength, we now fully model the wavelength response of each instrument. We have applied this improved code to FLS 3, and find that the resulting changes in the model parameters are well within the quoted uncertainties.

<div align="center">REFERENCES</div>

Alexander, D. M. et al. 2003, AJ, 126, 539
Alexander, D. M. et al. 2005, ApJ, 632, 736
Amblard, A. et al. 2011, Nature, 470, 510
Aretxaga, I. et al. 2011, MNRAS, 415, 3831
Astropy Collaboration 2013, A&A, 558, A33
Austermann, J. E. et al. 2010, MNRAS, 401, 160
Barger, A. J., Cowie, L. L., Sanders, D. B., Fulton, E., Taniguchi, Y., Sato, Y., Kawara, K., & Okuda, H. 1998, Nature, 394, 248
Baugh, C. M., Lacey, C. G., Frenk, C. S., Granato, G. L., Silva, L., Bressan, A., Benson, A. J., & Cole, S. 2005, MNRAS, 356, 1191
Becker, R. H., White, R. L., & Helfand, D. J. 1995, ApJ, 450, 559
Bendo, G. J. et al. 2013, ArXiv e-prints, accepted for publication in MNRAS
Bertoldi, F. et al. 2007, ApJS, 172, 132
Béthermin, M. et al. 2012, ApJ, 757, L23
Béthermin, M., Dole, H., Lagache, G., Le Borgne, D., & Penin, A. 2011, A&A, 529, A4
Blain, A. W., Barnard, V. E., & Chapman, S. C. 2003, MNRAS, 338, 733
Blain, A. W. & Longair, M. S. 1993, MNRAS, 264, 509
Blain, A. W. et al. 2002, Phys. Rep., 369, 111
Borys, C. et al. 2003, MNRAS, 344, 385
Bouwens, R. J. et al. 2007, ApJ, 670, 928
Capak, P. L. et al. 2011, Nature, 470, 233
Capozzi, D. et al. 2012, MNRAS, 419, 2821
Casey, C. M. et al. 2012, ApJ, 761, 140
Chapin, E. L. et al. 2011, MNRAS, 411, 505
Chapman, S. C., et al. 2005, ApJ, 622, 772
Clements, D. L. et al. 2010, A&A, 518, L8
Combes, F. et al. 2012, A&A, 538, L4
Condon, J. J., et al. 1998, AJ, 115, 1693
Conley, A. et al. 2011, ApJ, 732, L35
Coppin, K. E. K. et al. 2009, MNRAS, 395, 1905
Coppin et al., K. 2006, MNRAS, 372, 1621
Cox, P. et al. 2011, ApJ, 740, 63
Daddi, E. et al. 2009, ApJ, 695, L176
Dannerbauer, H. et al. 2002, ApJ, 573, 473
Diolaiti, E. et al. 2000, Astron. and Astrophysics Suppl., 147, 335
Draine, B. T. 2006, ApJ, 636, 1114
Dunne, L., Eales, S. A., & Edmunds, M. G. 2003, MNRAS, 341, 589
Eales, S. et al. 2010, PASP, 122, 499
Eales, S. et al. 2000, AJ, 120, 2244
Earle, L. et al. 2006, in Presented at the Society of Photo-Optical Instrumentation Engineers (SPIE) Conference, Vol. 6275, Society of
    Photo-Optical Instrumentation Engineers (SPIE) Conference Series
Fernandez-Conde, N., et al. 2008, A&A, 481, 885
Fixsen, D. J. et al. 1998, ApJ, 508, 123
Foreman-Mackey, D. et al. 2013, PASP, 125, 306
Franceschini, A. et al. 2010, A&A, 517, A74+
Fu, H. et al. 2013, Nature, 498, 338
Glenn, J. et al. 2003, in Society of Photo-Optical Instrumentation Engineers (SPIE) Conference Series, Vol. 4855, Society of
    Photo-Optical Instrumentation Engineers (SPIE) Conference Series, ed. T. G. Phillips & J. Zmuidzinas, 30–40
Glenn, J. et al. 2010, MNRAS, 409, 109
Greve, T. R. et al. 2004, MNRAS, 354, 779
Greve, T. R. et al. 2012, ApJ, 756, 101
Griffin, M. J. et al. 2010, A&A, 518, L3+
Hayward, C. C. et al. 2013, MNRAS, 428, 2529
Hodge, J. A. et al. 2013, ApJ, 768, 91
Hughes, D. H. et al. 1998, Nature, 394, 241
Ivison, R. J. et al. 2007, MNRAS, 380, 199
Ivison, R. J. et al. 2010, A&A, 518, L31
Kaviraj, S. et al. 2013, MNRAS, 428, 925
Kennicutt, Jr. 1998, ApJ, 498, 541
Kovács, A. et al. 2006, ApJ, 650, 592
Lagache, G. et al. 2004, ApJS, 154, 112
Lagache, G., Puget, J.-L., & Dole, H. 2005, ARA&A, 43, 727
Laurent, G. T. et al. 2005, ApJ, 623, 742
Le Borgne, D. et al. 2009, A&A, 504, 727
Levenson, L. et al. 2010, MNRAS, 409, 83
Lupu, R. E. et al. 2012, ApJ, 757, 135
Marsden, D. et al. 2013, ArXiv e-prints
Magnelli, B. et al. 2012, A&A, 539, A155
Michałowski, M. J. et al. 2012, MNRAS, 426, 1845
Mocanu, L. M. et al. 2013, ArXiv e-prints

Morrison, G. E. et al. 2010, ApJS, 188, 178
Negrello, M. et al. 2007, MNRAS, 377, 1557
Nguyen, H. T. et al. 2010, A&A, 518, L5+
Oke, J. B. et al. 1995, PASP, 107, 375
Oliver, S. J. et al. 2010, A&A, 518, L21
Oliver, S. J. et al. 2012, MNRAS, 424, 1614
Owen, F. N. & Morrison, G. E. 2008, AJ, 136, 1889
Perera, T. A. et al. 2008, MNRAS, 391, 1227
Pilbratt, G. L. et al. 2010, A&A, 518, 1
Pope, A. et al. 2005, MNRAS, 358, 149
Rangwala, N. et al. 2011, ApJ, 743, 94
Richards, G. T. et al. 2009, AJ, 137, 3884
Riechers, D. A. et al. 2013, Nature, 496, 329
Riechers, D. A. et al. 2010, ApJ, 720, L131
Roseboom, I. G. et al. 2010, MNRAS, 409, 48
Schwartz, P. R. 1982, ApJ, 252, 589
Scott, K. S. et al. 2008, MNRAS, 385, 2225
Scott, S. E. et al. 2002, MNRAS, 331, 817
Smail, I., Ivison, R. J., & Blain, A. W. 1997, ApJ, 490, L5+
Smith, A. J. et al. 2012, MNRAS, 419, 377
Sobral, D. et al. 2012, MNRAS, 420, 1926
Stott, J. P. et al. 2011, MNRAS, 414, 445
Swinbank, A. M. et al. 2012, MNRAS, 427, 1066
Swinbank, A. M. et al. 2010, Nature, 464, 733
Valiante, E. et al. 2009, ApJ, 701, 1814
Vieira, J. D. et al. 2013, Nature, 495, 344
Viero, M. P. et al. 2012, ArXiv e-prints, accepted for publication in ApJ
Walter, F. et al. 2012, Nature, 486, 233
Wardlow, J. L. et al. 2013, ApJ, 762, 59
Weiß, A. et al. 2013, ApJ, 767, 88
Weiß, A. et al. 2009, ApJ, 707, 1201
Wu, J. et al. 2012, ApJ, 756, 96
Xu, C. et al. 2001, ApJ, 562, 179
Younger, J. D. et al. 2007, ApJ, 671, 1531
Younger, J. D. et al. 2009, ApJ, 704, 803